Flame structure analysis and composition space modeling of thermodiffusively unstable premixed hydrogen flames — Part II: Elevated pressure

Xu Wen[a,*], Thorsten Zirwes[b,c], Arne Scholtissek[a], Hannes Böttler[a], Feichi Zhang[c], Henning Bockhorn[c], Christian Hasse[a]

[a]*Simulation of Reactive Thermo-Fluid Systems, TU Darmstadt, Otto-Berndt-Straße 2, 64287 Darmstadt, Germany*
[b]*Steinbuch Centre for Computing, Karlsruhe Institute of Technology, Hermann-von-Helmholtz-Platz 1, 76344 Eggenstein-Leopoldshafen, Germany*
[c]*Engler-Bunte-Institute, Karlsruhe Institute of Technology, Engler-Bunte-Ring 7, 76131 Karlsruhe, Germany*

Abstract

This paper is a continuation of the work we carried out in Part I (Wen et al., 2021), studying the flame structure analysis and composition space modeling of an outwardly expanding thermodiffusively unstable premixed hydrogen flame at atmospheric pressure. In this work, we focus on the case of elevated pressure (5 atm), which is particularly challenging for the model proposed in Part I due to wider ranges of curvatures and strain rates induced by promoted intrinsic instabilities in the flame studied. A detailed chemistry simulation of the thermodiffusively unstable premixed hydrogen flame at 5 atm is first conducted, and the flame structure is comprehensively analyzed by comparing the simulation results with the asymptotic theory proposed by Matalon and co-workers (PCI, 2002; JFM, 2003). Then, budget terms of the generalized premixed flamelet equations are calculated to identify the dominating processes of the cells with different length scales. Finally, the performance of the proposed tabulation method based on premixed flamelet equations in composition space presented in Part I is evaluated through an *a priori* analysis by comparing tabulated values with the reference results. The critical flame radius and average cell size calculated with the asymptotic theory are found to agree well with the reference results. The calculated critical Péclet number at the elevated pressure is smaller than that under the condition of atmospheric pressure, suggesting a smaller critical flame radius as the pressure increases. The *budget* analysis shows that for either small- or large-scale cells, tangential diffusion is only important for flamelets with negative curvature. The *a priori* analysis shows that the proposed tabulation method per-

*Corresponding author:
Email address: wen@stfs.tu-darmstadt.de (Xu Wen)

forms well in predicting the intermediate species in regions with negative curvature, although the peak values of some species mass fractions are under-predicted. The reasons are explained and guidelines for future research to improve the model are outlined.
Keywords: Thermodiffusively unstable hydrogen flame, Flamelet tabulation, Elevated pressure, Strain, Curvature

1. Introduction

There is an increased interest in hydrogen as a chemical energy carrier, as reflected e.g. in the European Hydrogen Strategy [1]. Hydrogen has proven to have many desirable characteristics for use in gas turbines [2–4], and 100% hydrogen gas turbines are being developed [5]. For example, the wide range of hydrogen's flammability limit makes smooth engine operation possible, its high burning velocity enables a shorter combustion period and thus a relatively high thermal efficiency, and its lower requirement of spark energy for ignition enables a lower cyclic fluctuation. However, hydrogen combustion is extremely fast, which may induce knock, pre-ignition, etc., and the high burning velocity may result in flashback and thus strong heat losses. To avoid these problems and to improve the working efficiency and workload, the internal mixing of hydrogen is often equipped with a high-pressure injection system [6]. However, hydrogen combustion under high pressure conditions tends to be unstable. Previous numerical [7–9] and experimental [10–15] studies reported that flames with various fuel-air mixtures become intrinsically unstable with increasing pressure. For highly diffusive fuel species such as hydrogen, the intrinsic flame instability would be further pronounced due to the introduced thermodiffusive instability of a lower Lewis number [7, 11].

The influence of pressure on the flame stability is visually shown by the schlieren photography in Fig. 1, which are obtained at 8000 frames per second [16]. These are spherically expanding hydrogen/air flames operated under atmospheric (left) and engine-like (right) conditions. It is seen that in atmospheric conditions, an ideal stable and smooth flame surface can be obtained[1]. However, at an increased pressure, corrugations can be observed at the flame surface with a wide range of length scales due to enhanced hydrodynamic instability.

The effects of elevated pressure on flame instability have been investigated in several previous studies for specific fuel types and equivalence ratios, including theoretical analyses [17, 18], nu-

[1]For the fuel-rich condition studied ($\phi = 4$), the hydrogen/air flame is stable at the atmospheric condition.

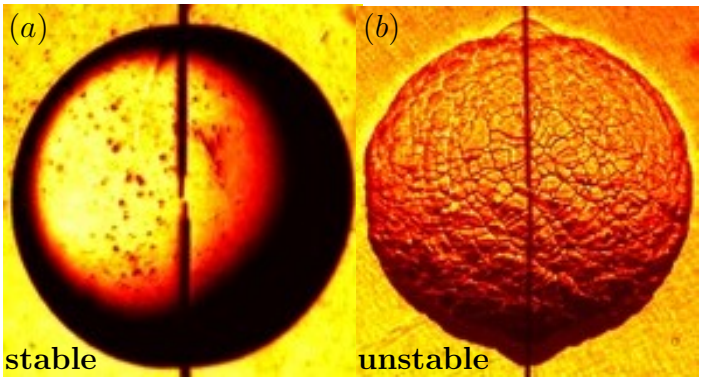

Fig. 1. Snapshots of a spherically expanding flame in different pressure conditions with the fuel-rich hydrogen/air mixture. The left flame corresponds to the ideal stable and smooth flame surface at an atmospheric pressure. The right flame is taken under elevated pressure in an internal combustion engine-like condition ($p = 40\,\mathrm{atm}$) [16].

merical simulations [7–9], and measurements [10–15, 19]. For the theoretical analysis, Darrieus [20] and Landau [21] independently proposed the hydrodynamic instability theory (D-L instability), which assumes that the flame is infinitesimally thin and propagates normal to the flame surface at a constant speed. The D-L model was further extended by Istratov and Librovich [22] with the Markstein correction, and later by Bechtold and Matalon [23], who consistently took into account the hydrodynamic and thermodiffusive effects. Matalon and co-workers [17, 18] finally generalized the model, which is valid for the whole range of equivalence ratios and allows for temperature-dependent transport properties. The derived asymptotic theory, which is valid for both atmospheric and elevated pressures, has been used to interpret numerical [7, 24–30] and experimental [11, 13, 15, 31] results. For intrinsically unstable flames operated under elevated pressure conditions, Law et al. [13] experimentally and theoretically investigated the effect on the cellular instabilities of expanding spherical flames for a mixture with a stabilizing species (propane) and a destabilizing species (hydrogen). They found that the critical Péclet number (the flame radius normalized by its thickness) obtained from the asymptotic theory proposed in [17] agrees reasonably well with the measured value for a range of pressures and mixture compositions. Beeckmann et al. [15] also conducted experimental and theoretical studies for outwardly propagating spherical hydrogen/air flames over a wide range of equivalence ratios, initial pressures and temperatures. The measured flame propagation speed shows good agreement with the asymptotic theory proposed by Addabbo et al. [17], with the chosen flame parameters of activation energy, flame thickness, etc., but the critical radii are considerably under-predicted by the asymptotic theory with the same flame parameters. Yuan et al. [7] numerically investigated the pressure effects on instability of

planar flames for both linear and non-linear stages when the effective Lewis number (Le) is less than or equal to unity. The simulation was conducted with an irreversible one-step reaction, and the predicted growth rate was compared to the linear dispersion relation derived by Matalon and Matkowsky [32]. They found that the theory can give qualitative predictions of the linear dispersion relation. Recently, Attili et al. [9] investigated the effect of pressure on the hydrodynamic stability of lean methane/air premixed planar flames with direct numerical simulation (DNS) based on both multi-step chemistry and a simplified one-step chemistry. They found that the decrease in the cut-off length, which separates stable from unstable wavelengths, cannot only be attributed to the decreased flame thickness due to elevated pressures: the increase in the Zeldovich number with growing pressure is also important. This can be related to the increase in the inner layer temperature with pressure due to pronounced chain termination reactions, leading the Zeldovich number to increase. From the above literature review, it is evident that the asymptotic theory is rarely used to study the DNS of a spherically expanding unstable lean hydrogen/air flame at elevated pressure, which is one of the purposes of this work.

Compared to the thermodiffusively unstable flame in atmospheric conditions, the promoted hydrodynamic instability at an elevated pressure results in wider ranges of curvatures and strain rates, which poses a particular challenge and enables the investigation of possible model limitations. The combustion model used in this work is based on a flamelet tabulation method [33, 34]. With the ultimate goal of simulating industrial applications, the flamelet model offers a promising advantage over other finite-rate combustion models since the detailed chemical reaction mechanism can be taken into account at a reasonable computational cost. With regard to flamelet modeling of differential diffusion, curvature and the strain rate, the relevant works have been reviewed in the first part of this series [35]. Here, the works on flamelet modeling of flames under elevated pressures are briefly reviewed. Bekdemir et al. [36] adopted a pressure-dependent Flamelet Generated Manifolds [37] for modeling diesel engine combustion. To examine how pressure variations affect the ignition process, a flamelet table with several pressure levels was generated, and pressure was introduced as one of the trajectory variables. It was found that the global diesel combustion characteristics such as the flame lift-off observed in experiments can be qualitatively predicted with the developed flamelet model. Mittal and Pitsch [38] also proposed a flamelet tabulation method to adapt to pressure variations in internal combustion engines. Instead of choosing pressure itself as one of the trajectory variables to avoid high memory requirement, the flamelet table is generated only at a reference pressure. The thermo-chemical quantities at the other pressure

values are obtained using a quadratic logarithmic expansion in pressure. The model was validated by comparing against DNS data under isochoric conditions, and it was shown that the variable pressure effect on temperature can be captured. Ladeinde et al. [39] compared the above two techniques and found that introducing pressure as one of the trajectory variables performs better for supersonic combustion. However, we note that these studies focus on pressure variations in stable flames, without differential diffusion, curvature and strain rate effects being explicitly considered. It is still unclear whether the flamelet model works for the intrinsically unstable flame at an elevated pressure.

In Part I [35], a new flamelet tabulation method was proposed based on the self-contained strained-curved flamelet equations in composition space, aiming at addressing the recurring issues when modeling differential diffusion, the strain rate and curvature. The suitability of the new flamelet tabulation method was evaluated on a thermodiffusively unstable flame at atmospheric condition. This work is a continuation of Part I [35], and the focus here is on the conditions at an elevated pressure. The purpose of the present work includes the following aspects:

(i) Flame structure analysis: Detailed chemistry simulation of an outwardly expanding lean premixed hydrogen flame is conducted at an elevated pressure (5 atm), involving strong hydrodynamic and thermodiffusive instabilities, and using detailed transport properties and chemical reaction mechanism. The differences between the thermodiffusively unstable flames at different pressure conditions are analyzed and quantified, including both macroscopic and microscopic properties, e.g., cell size, flame front curvature, Bilger mixture fraction, etc.;

(ii) Comparison to asymptotic theory: The asymptotic theory proposed by Matalon and coworkers [17, 18] is used to analyze the reference solutions at different pressure conditions. Particularly, the critical wavelength (i.e., cell size) and Péclet number (i.e., flame radius) obtained from the theory are compared to those extracted from the reference solutions;

(iii) *Budget* analysis: Compared to the atmospheric pressure condition, the hydrodynamic and thermodiffusive instabilities at the elevated pressure condition are expected to be stronger. A *budget* analysis of the generalized premixed flamelet equations is conducted to identify the important processes in the strongly corrugated cellular structures, and to clarify the differences with the thermodiffusively unstable flame at atmospheric condition in the local microstructure and how such differences influence the performance of the flamelet models. In the *budget* analysis, the budget terms in the generalized premixed flamelet equations are

calculated from the reference solutions, and then compared with each other;

(iv) *A priori* analysis: For thermodiffusively unstable premixed hydrogen flames, the strain rate and curvature span wider ranges as the pressure increases, pushing the flamelet manifold method to its limit. The performance of the flamelet tabulation method proposed in Part I [35] will be further evaluated through an *a priori* analysis to identify its strengths and limitations. In the *a priori* analysis, the trajectory variables in the flamelet tabulation method are calculated from the reference solutions, and then the tabulated values are compared to the corresponding reference solutions.

The remainder of the paper is organized as follows: In Section 2, the numerical setup of the premixed hydrogen flame at an elevated pressure is presented. The modeling approach is given in Section 3. Results and discussions are given in Section 4. In the last section, the main findings obtained in this work are summarized.

2. Numerical approach

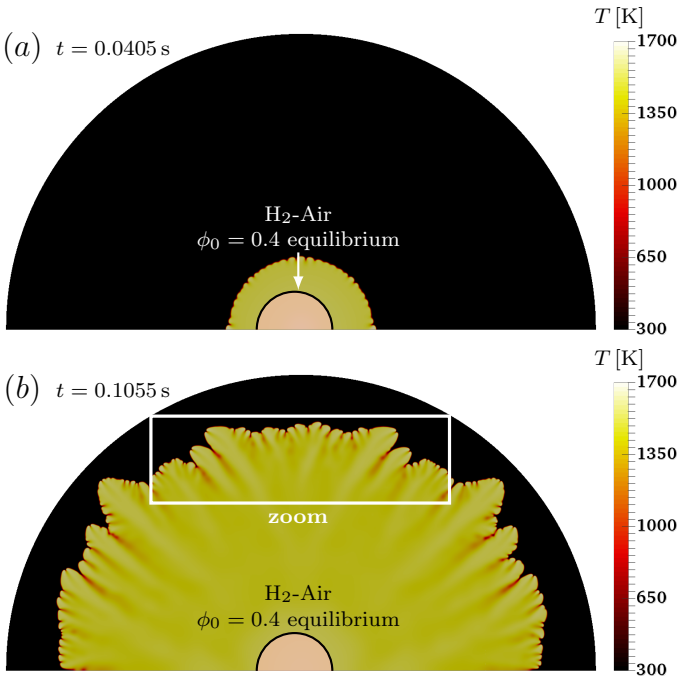

Fig. 2. Instantaneous distributions of the gas temperature for the thermodiffusively unstable H_2/air flame at (a) the early transition state ($t = 0.0405\,\mathrm{s}$) and (b) the later fully unstable state ($t = 0.1055\,\mathrm{s}$) at a pressure of 5 atm, an unburnt mixture equivalence ratio of 0.4 and a temperature of 300 K. The initial states in the center of the domain are indicated. The zoomed region indicated in (b) will be investigated in detail in Section 4.

In this work, a detailed chemistry simulation for the thermodiffusively unstable premixed hy-

drogen flame at elevated pressure is conducted to analyze the flame structure and evaluate the performance of the flamelet tabulation method. The same as in Part I [35] for atmospheric conditions, the adopted computational domain is a wedge in the Cartesian coordinates: it is 2D as in previous works [7, 9, 18, 26, 28, 30, 40–43] and covers a half-sphere with a radius of 0.08 m, see Fig. 2. For the outwardly expanding flame studied in this work, the 2D approximation is considered to be suitable as the flame mainly propagates towards the radial direction. Besides, as sufficiently fine mesh resolution is required to resolve the flame structure and a relatively large computational domain is required to allow the formation of the finger-like cellular structure, 2D configuration is a good compromise between computational efficiency and accuracy. The 2D configuration for the outwardly propagating unstable premixed flame was also used in previous studies [40, 42]. The center of the domain with a radius of 0.01 m is initialized with the burnt products of H_2/air at the equivalence ratio of 0.4 and the pressure of 5 atm, while the other parts of the domain are initialized with an unburnt mixture of H_2/air at the same equivalence ratio and pressure. The temperature of the unburnt mixture is set to 300 K. Instantaneous distributions of the temperature at the early transition state and the later fully unstable state are shown in Fig. 2 to illustrate the expansion of the premixed flame under high pressure. In the x and z directions, 9000 and 14400 grid points are set with local refinement, resulting in a total of 32.4 M cells. In the rectangular region in the center of the domain with $100\,\mathrm{mm}(z) \times 50\,\mathrm{mm}(x)$, an equidistant resolution with $16\,\mu$m is used, while outside this region, an equidistant resolution with $20\,\mu$m is utilized. So, around 24 grid points are used to resolve the laminar flame thickness through all time instants. The mesh resolution is evaluated by comparing the profiles of the species mass fractions and temperature obtained from the reference solutions against the corresponding quantities from the 1D freely propagating premixed flame calculated using the ULF package [44]. Further, the quality of the mesh resolution is confirmed since the same results are obtained using half of the grid points in each direction. Zero-gradient boundary condition is set for all the variables along the outer boundary, while the wedge boundary condition is set for all the variables at the patch pair in the y direction.

In the reference solutions, the governing equations for the species mass fractions and sensible enthalpy in their fully compressible formulation are solved using a solver [45–48] developed based on the open-source code OpenFOAM [49]. In order to calculate the detailed molecular diffusion coefficients and the finite reaction rates from the detailed chemistry mechanism, the flow solver is coupled with the open-source library Cantera [50]. The details of the governing equations are described in our previous works [47, 48], and are not repeated here for simplicity. The diffusion flux

is calculated with the mixture-averaged approach (detailed molecular diffusion with Hirschfelder-Curtiss approximation [51]) with the Soret effect being neglected as in recent DNS studies for the intrinsically unstable planar flames [9, 28]. The chemical reaction mechanism developed by Varga et al. [52] (12 species and 29 elementary reactions) is utilized in the reference solutions. A second-order backward scheme is used for the time discretization, while a fourth-order interpolation scheme is employed for the spatial discretization. The time-step is calculated according to the Courant number, which is set at 0.1 to ensure the stability and accuracy of the simulation.

3. Modeling approach

In this section, the techniques of the *budget* analysis, the *a priori* analysis, and the linear stability analysis are presented.

3.1. Budget analysis of generalized premixed flamelet equations in composition space

The detailed formulation of the premixed flamelet equations in composition space with the strain rate and curvature derived by Scholtissek et al. [53] was presented in Part I [35]. To facilitate the description of the analysis techniques, the generalized premixed flamelet equations in composition space for the species mass fraction Y_i and temperature T are given as follows,

$$\Lambda^{Y_i}_{\text{tran}} = \Lambda^{Y_i}_{\text{diff}} + \Lambda^{Y_i}_{\text{conv}} + \Lambda^{Y_i}_{\text{curv}} + \Lambda^{Y_i}_{\text{TD}} + \Lambda^{Y_i}_{\text{src}} \tag{1}$$

$$\Lambda^{T}_{\text{tran}} = \Lambda^{T}_{\text{diff}} + \Lambda^{T}_{\text{conv}} + \Lambda^{T}_{\text{curv}} + \Lambda^{T}_{\text{TD}} + \Lambda^{T}_{\text{src}} \tag{2}$$

where Λ_{tran} is the transient term, Λ_{diff} the diffusion normal to the flame front, Λ_{conv} the convection term, Λ_{curv} the curvature term, Λ_{TD} the diffusion along the flame front, and Λ_{src} the reaction source term. Note that in 1D flamelet solutions, the tangential diffusion (TD) term Λ_{TD} is not included. It is included in Eqs. (1) and (2) purely to ensure the balance for the *budget* analysis.

Budget analysis can be used to identify the importance of different physical processes, i.e., the transient phenomenon, normal diffusion, tangential diffusion, convection, curvature and reaction rate. Compared to atmospheric conditions, the flame front appears strongly corrugated over a wider range of length scales at the elevated pressure due to enhanced hydrodynamic instability. Thus, it is interesting to investigate whether the importance of different processes, particularly related to curvature and tangential diffusion, changes as the pressure increases.

3.2. A priori analysis of the flamelet tabulation method

This subsection presents the flamelet tabulation method used to analyze the thermodiffusively unstable premixed hydrogen flame at high pressure.

The flamelet table is generated by solving the strained-curved flamelet equations, see Eqs. (1) and (2), without the transient Λ_{tran} and the tangential diffusion Λ_{TD} terms. Note that the species mass fraction and temperature governing equations, i.e., Eqs. (1) and (2), in composition space are not closed, and an additional governing equation for the gradient of the composition space must be solved [53, 54]. To cover the wide ranges of the curvature κ_c and strain rate K_s in the thermodiffusively unstable flame, the flamelet equations are solved for various values of κ_c and K_s. The parameters κ_c and K_s are respectively defined as $\kappa_c = -\nabla \cdot \overrightarrow{n} = -\nabla \cdot (\nabla Y_{PV}/|\nabla Y_{PV}|)$ and $K_s = \nabla_t \cdot \overrightarrow{u_t} - (\overrightarrow{u} \cdot \overrightarrow{n})\,\kappa_c$, where $\overrightarrow{u_t}$ is the tangential component of fluid velocity $\overrightarrow{u}$, and Y_{PV} the reaction progress variable. For the hydrogen/air flame studied in this work, Y_{PV} is defined as $Y_{PV} = Y_{\text{H}_2\text{O}} - Y_{\text{O}_2} - Y_{\text{H}_2}$ as in previous publications [53–55]. Due to the existence of stratification induced by differential diffusion, the flamelet equations in composition space are solved for various equivalence ratios of the fresh H_2/air mixture, ranging from 0.35 to 0.5 to cover the whole range of equivalence ratios in the reference solutions created by differential diffusion. The temperature and pressure of the fresh fuel mixture are set to 300 K and 5 atm, respectively, corresponding to the reference simulation setup. To maintain consistency with the reference simulation, the same method is used to calculate the diffusion flux, see Section 2. The premixed flamelet equations in composition space are solved using the in-house code ULF [44].

As already demonstrated in Part I [35], the curvature κ_c and strain rate K_s themselves are not the ideal trajectory variables to tabulate the thermo-chemical quantities. Instead, the thermo-chemical quantities have to be mapped to the reacting variable space. To this end, it is required to identify the variables that can characterize the flame structure's internal response to the strain rate and curvature. The results obtained from the flamelet solutions at the elevated pressure are given in the Supplementary Material.

Based on the findings obtained from the flamelet solutions for the H_2/air flame at high pressure, the thermo-chemical values in the strained-curved flame can be tabulated as follows,

$$\Psi = \Psi^{\text{MAP}}\left(Z_{\text{Bilger}}, Y_{PV}, Y_{\text{H}}^{\text{str}}, Y_{\text{H}}^{\text{curv}}\right) \tag{3}$$

where Z_{Bilger} is introduced to characterize the differential diffusion, Y_{PV} is used to describe the progress of reactions, and $Y_{\text{H}}^{\text{str}}$ and $Y_{\text{H}}^{\text{curv}}$ are utilized to represent the flame structure's internal

response to the strain rate and curvature, respectively. Here, the superscripts $(\cdot)^{\mathrm{str}}$ and $(\cdot)^{\mathrm{curv}}$ are introduced to differentiate the Y_{H} that characterizes the strain rate and curvature, respectively. We note that both $Y_{\mathrm{H}}^{\mathrm{str}}$ and $Y_{\mathrm{H}}^{\mathrm{curv}}$ must be kept in Eq. (3), since they are mapped from two independent parameters of the strain rate and curvature, respectively.

In order to confirm the advantages of the new tabulation method based on the strained-curved flamelet equations, the conventional flamelet model based on the 1D freely propagating premixed (FPP) flame is introduced for comparison. In the FPP flamelet model, the 1D flamelet equations in physical space are solved for various equivalence ratios, covering the whole range in the reference solutions. Again, the diffusion flux is calculated with the same method as the reference simulation for consistency. The flamelet solutions obtained can be parameterized as follows,

$$\Psi = \Psi^{\mathrm{FPP}}\left(Z_{\mathrm{Bilger}}, Y_{PV}\right) \tag{4}$$

where Z_{Bilger} is introduced to characterize the differential diffusion, while Y_{PV} is used to describe the progress of reactions. Note that Z_{Bilger} is the local value through the flame, but not the value in the fresh gases. As can be seen, the effects of strain rate and curvature are not explicitly taken into account in the FPP flamelet table.

3.3. Linear stability analysis from asymptotic theory

For the expanding flame investigated in this work, the perturbed flame front can be expressed as $r = R(t)\left[1 + A(t)S_n\left(\theta, \phi\right)\right]$, with $R(t)$ the flame radius at time t, $A(t)$ the amplitude of the disturbance, and S_n the spherical surface harmonics with n the wavenumber. As described by Addabbo et al. [17], it is the growth/decay of $A(t)$ that determines the flame stability or instability. The growth rate of a disturbance with wavenumber n can be determined as

$$\frac{1}{A}\frac{\mathrm{d}A}{\mathrm{d}t} = \frac{\dot{R}}{R}\left(\omega_{DL} - \frac{l_D}{R}\Omega\right)\Bigg|_n \tag{5}$$

where $\dot{R}$ represents the flame propagation speed (here the dot represents differentiation with respect to time), and l_D the diffusion length, defined as $l_D \equiv D_{th}/S_L = \lambda_u/(\rho_u c_{p,u} S_L)$, with λ_u, ρ_u and $c_{p,u}$ the thermal conductivity, density and heat capacity of the unburnt mixture. S_L is the laminar burning velocity, and the variables ω_{DL} and Ω are functions of the thermal expansion σ, the effective Lewis number Le_{eff}, the Prandtl number Pr, and the wavenumber n [17],

$$\omega_{DL} = \left[-\left(b-a\right) + \sqrt{\left(b-a\right)^2 - 4ac}\right]/2a \tag{6a}$$

$$\Omega = \Omega_1 + \left[\mathscr{Z}\left(Le_{eff} - 1\right)/\left(\sigma - 1\right)\right]\Omega_2 + Pr\Omega_3 \tag{6b}$$

where $\mathscr{Z}$ is the Zeldovich number, defined as $\mathscr{Z} = E\left(T_a - T_u\right)/\left(R^0 T_a^2\right)$, E the activation energy, T_a the adiabatic flame temperature, T_u the temperature of the unburnt fuel mixture, and R^0 the gas constant. The formulations of a, b and c for calculating ω_{DL} depend only on the thermal expansion σ $(= T_a/T_u = \rho_u/\rho_b)$ and wavenumber n. Thus, ω_{DL} represents the instability due to thermal expansion, i.e., the Darrieus-Landau instability. The coefficients of Ω_1, Ω_2 and Ω_3 represent the effects of thermal diffusion, molecular diffusion, and viscous diffusion, respectively. The definitions of a, b, c, Ω_1, Ω_2 and Ω_3 can be found in ref. [17]. For completeness, we provide the formulations utilized in this work in the Supplementary Material.

3.3.1. Critical Péclet number and wavenumber

From Eq. (5), it is clear that the flame is stable at a given time instant if the growth rate is negative for all wavenumbers, while it becomes unstable if the growth rate is positive for at least one wavenumber. Thus, the combined diffusion effects may stabilize or destabilize the flame, depending on whether Ω is positive or negative. The neutral stability state can be obtained by setting the right-hand side of Eq. (5) to zero,

$$Pe = \frac{R}{l_D} = \frac{\Omega}{\omega_{DL}} = \frac{\mathscr{F}(n)}{\mathscr{G}(n)} \tag{7}$$

where Pe is the Péclet number, defined as the ratio of the instantaneous flame radius R to the diffusion length l_D. The flame becomes unstable when its radius exceeds the critical value R_c, i.e., the critical Péclet number Pe_c. Considering that both Ω and ω_{DL} are functions of the wavenumber, indicated by the last relation in Eq. (7), the critical wavenumber n_c can be determined according to the critical Péclet number Pe_c in the n-Pe space.

3.3.2. Critical cell size

In the n-Pe space, for a given Péclet number larger than Pe_c, a range of unstable wavenumbers, $n_{min} < n < n_{max}$, can be found for an unstable flame, see Fig. 7a. For a stable flame with $n < n_{min}$, the wavelength $\Lambda = 2\pi R/n$ is so long that the extremely large cell size on the flame surface is stretched out by the expanding flame. In contrast, for a stable flame with $n > n_{max}$, the wavelength is so short that the sufficiently small cell size on the flame surface tends to smooth out the differences in the temperature and concentration.

The asymptotic value of the wavenumber according to the lower branch of the neutral stability curve from Eq. (7), n^*_{min}, can be obtained by setting $Pe \to \infty$, i.e., $\omega_{DL} = 0$. From Eq. (6a), it is

clear that n^*_{min} is only a function of σ; it is independent of the equivalence ratio, effective Lewis number and Prandtl number. This is a consistent result since the lower branch corresponds to the hydrodynamic instability, which is purely dependent on the thermal expansion. According to the determined lower limit of n^*_{min}, the largest cell size can be calculated as $\Lambda_{max} = 2\pi R/n^*_{min}$.

On the other hand, it can be calculated that the asymptotic value of the wavenumber n^*_{max}, according to the upper branch of the neutral stability curve, approaches the line $Pe/n^*_{max} = \Gamma$, with Γ being

$$\Gamma = \left[C_1 + \beta\left(Le_{eff} - 1\right)C_2 + PrC_3\right]/C_4 \tag{8}$$

The complete formulations for C_1, C_2, C_3 and C_4 are provided in the Supplementary Material. According to the asymptotic line of the upper branch, the smallest cell size can be calculated as $\Lambda_{min} = 2\pi R/n^*_{max} = 2\pi l_D\Gamma$. As pointed out by Addabbo et al. [17], Λ_{min} can be used to represent the average cell size because smaller cells cannot survive when the whole flame surface becomes cellular.

In this work, the critical flame radius and the critical cell size obtained from the asymptotic theory are compared to the values extracted from the reference solutions to interpret the flame instability.

4. Results and discussions

In Section 4.1, the structure of the thermodiffusively unstable flame is described. Then, a *budget* analysis (Section 4.2) of the generalized premixed flamelet equations is conducted. Finally, an *a priori* analysis (Section 4.3) is conducted to evaluate the performance of the proposed flamelet tabulation method in predicting the strained-curved flame at elevated pressure.

4.1. Structure of the thermodiffusively unstable flame

The structure of the thermodiffusively unstable flame at the elevated pressure is analyzed in this subsection.

Figure 3 shows the instantaneous distributions of the OH mass fraction Y_{OH}, the Bilger mixture fraction Z_{Bilger}, the strain rate K_s, and the curvature κ_c. Only a certain region around the flame front, as indicated in Fig. 2b, is shown, to highlight the cellular structure of the thermodiffusively unstable flame. It can be observed that the flame front is strongly corrugated over a wide range of length scales ($\mathscr{L}$). Compared to the flame front with the same flame radius under atmospheric conditions, the range of length scales at elevated pressure becomes much wider. This is because the

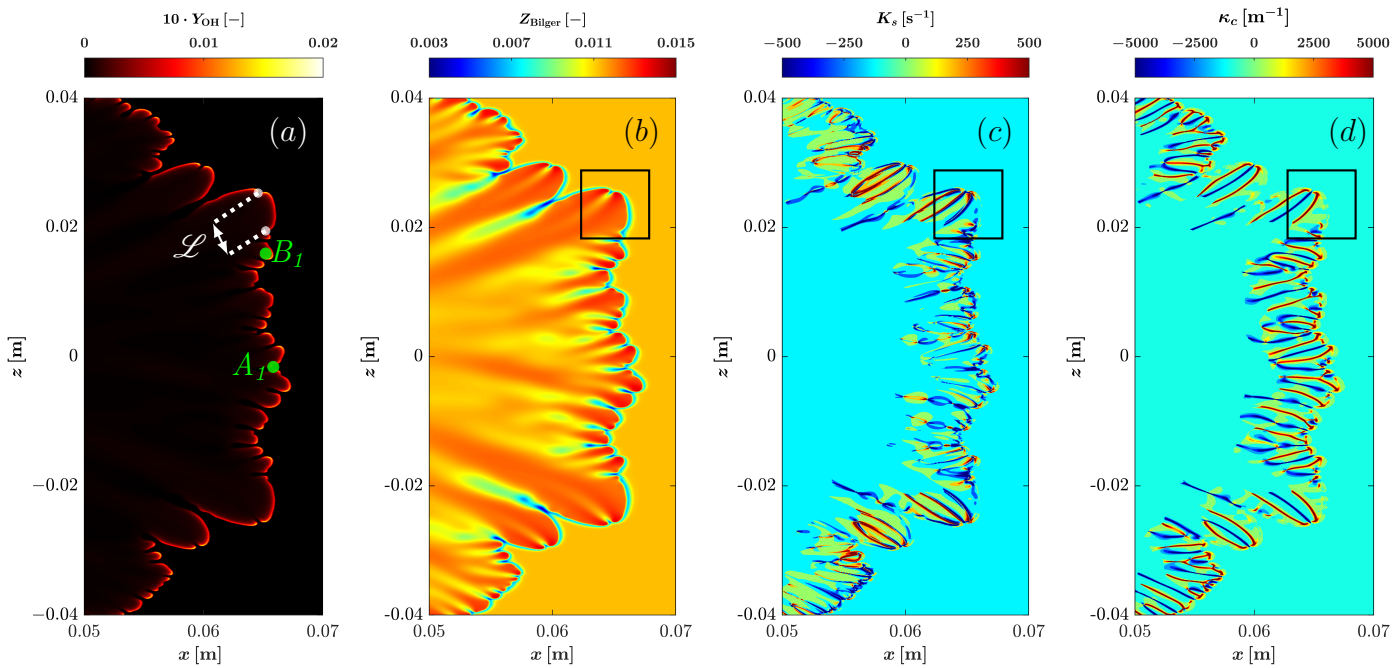

Fig. 3. Instantaneous distributions of the (a) OH mass fraction, (b) Bilger mixture fraction, (c) strain rate, and (d) flame front curvature at a pressure of 5 atm in the selected region indicated in Fig. 2. A region with cellular flame structure is indicated as a box in (b)-(d). Point A_1 and point B_1 indicate the start and end locations of the flame front that will be investigated through an *a priori* analysis in Section 4.3. The strain rate and curvature are calculated by conditioning on the reaction zone.

range of unstable wavenumbers increases for higher pressures, as described below by the asymptotic theory. Thus, a wide range of wavelengths (cell sizes) can grow at high pressure during the non-linear flame surface evolution. From Fig. 3a, it is also seen that at the location with negative curvature, see Fig. 3d, the concentration of OH is small, and local extinction occurs. In contrast, the concentration of OH is significantly larger at the location with positive curvature. The Bilger mixture fraction shown in Fig. 3b indicates significant stratification around the flame front and in the wake regions downstream. In general, a fuel-leaner ($\phi < 0.4$) wake region is obtained for a concavely curved flame front towards the unburnt mixture, while a fuel-richer ($\phi > 0.4$) wake region is formed for a convexly curved flame front. This phenomenon results from the faster diffusion velocity of hydrogen compared to the other species, which leads to fuel accumulating at the convexly curved flame front with a relatively smaller surface area.

Figure 3c shows the instantaneous distribution of the strain rate in the vicinity of the flame front. Note that both the strain rate and curvature are only shown for the reaction zone, defined as $\dot{\omega}_{H_2O} > 0$. Overall, the distribution of the strain rate is extremely complex in the cellular structure;

it is hard to relate the sign of the strain rate to the curvature distribution shown in Fig. 3d from the contour plots. The relations between the curvature, strain rate and Bilger mixture fraction along the flame front are clarified below. Compared to the thermodiffusively unstable flame under atmospheric conditions, the more complex cellular structure at elevated pressure might change the importance of tangential diffusion, a question which is clarified in the next subsection by means of a *budget* analysis.

To quantify the relations between the curvature, strain rate and Bilger mixture fraction further, a representative cellular structure shown in Fig. 4 is studied, which is around the region of interest marked in Fig. 3. Figure 4a and 4b show the contour plots of Y_{OH} and κ_c, while Fig. 4c-4e display the values along the flame front from the starting point to the end point, as indicated in the contour plot of Y_{OH}. The flame front is measured by the arc length l_{arc}, which is calculated along the flame front according to $l_{arc}^{(n+1)} = l_{arc}^{(n)} + \sqrt{(\mathrm{d}x)^2 + (\mathrm{d}z)^2}$, with n being the point index along the Y_{PV}-isoline. The starting point to calculate l_{arc}, i.e., $n = 0$, is the minimum values of x and z. The flame front is represented by the iso-line of $Y_{PV} = -0.11$, which crosses the location of peak Y_{H} in the selected region. Representative points at the cusps with negative curvature along the sample line are indicated, see points A, B, B_C^*, and C. The vertical dashed line indicates a location with a local peak of distinct negative curvature. One initial observation is that all the variables change significantly along the flame front, demonstrating the complicated flame structure of the unstable flame at the elevated pressure. It can also be clearly seen that the trends are closely correlated with each other. For example, the peak of the negative curvature corresponds to the peak of the positive strain rate, see the indicated positions in the figure. It is seen that this is also the region where Z_{Bilger} is small, which is a direct effect of differential diffusion, as expected for a lean H_2 flame. It is interesting to note that even for a small change in the curvature, indicated as point B_C^*, the strain rate and the Bilger mixture fraction have prompt responses, i.e., an increase in the strain rate and a decrease in the Bilger mixture fraction. Comparing the different cell sizes, we find that the curvature magnitude in the small cell is larger than that in the large cell, see point A and point C. In contrast, the corresponding strain rate in the large cell is much more significant than that in the small cell. To investigate the relations between the curvature and reaction rate, the profile of progress variable source term $\dot{\omega}_c$ is shown in Fig. 4f. It is clearly seen that at points A, B and C with significant negative curvature, the corresponding value of $\dot{\omega}_c$ is zero, indicating local extinction. In contrast, the reaction rate is significant at locations with positive curvature. This is due to the reason that the highly diffusive species, e.g., H_2, with strong differential diffusion tend

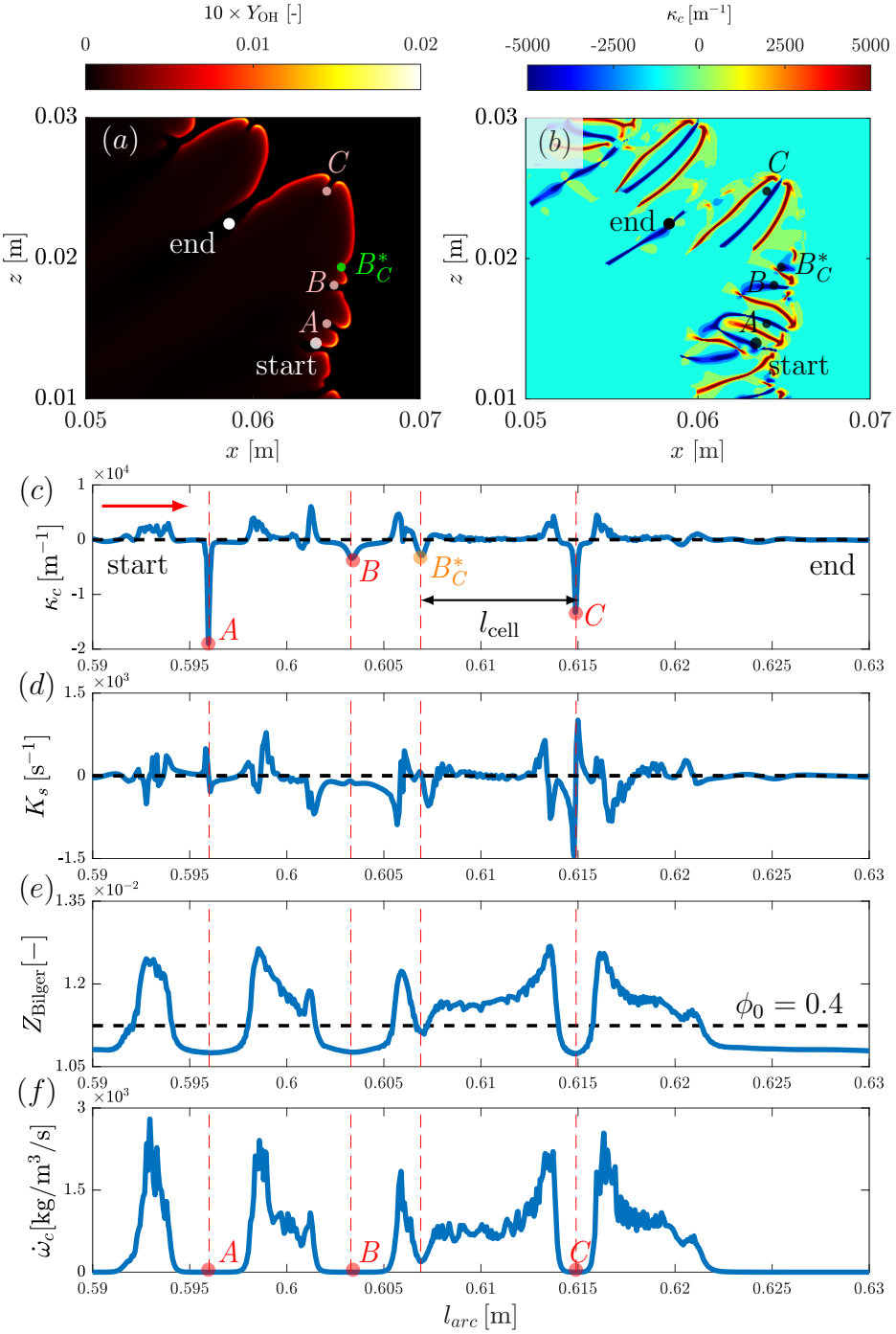

Fig. 4. (a,b) Contour plots of Y_{OH} and κ_c in a selected region to show the representative cell structure. The representative points at the cusps of the flame front are indicated in the contour plot of Y_{OH}. (c-f) The instantaneous distributions of the curvature, strain rate, Bilger mixture fraction and the progress variable source term along the flame front, which is measured by the arc length, $l_{arc}^{(n+1)} = l_{arc}^{(n)} + \sqrt{(\mathrm{d}x)^2 + (\mathrm{d}z)^2}$, with n being the point index along the Y_{PV}-isoline. The starting point and the end point are indicated in the contour plot of Y_{OH}. The vertical dashed line indicates a location with a peak of negative curvature. Points A, B and C indicate the locations with significant negative curvature that leads to local extinctions, i.e., $\dot{\omega}_c = 0$, as shown in (f). Point B^*_C indicates the local peak between B and C. The horizontal dashed line in (c) and (d) indicates the locations of $\kappa_c = 0$ and $K_s = 0$, respectively, while that in (e) indicates the location of $Z_{\mathrm{Bilger}} = 0.0112$, corresponding to the fresh H_2/air mixture in reference simulation, i.e., $\phi_0 = 0.4$.

to accumulate in the positively curved region with small flame surface, which leads to a fuel-richer mixture ($\phi > \phi_0 = 0.4$), as shown in Fig. 4e. The higher equivalence ratio corresponds to higher reaction rate and consumption speed. In contrast, in the negatively curved region, the highly diffusive species have to "fill in" the larger pit, which leads to a fuel-leaner mixture ($\phi < \phi_0 = 0.4$), as shown in Fig. 4e, corresponding to lower (or zero for extinguished locations) reaction rate and consumption speed.

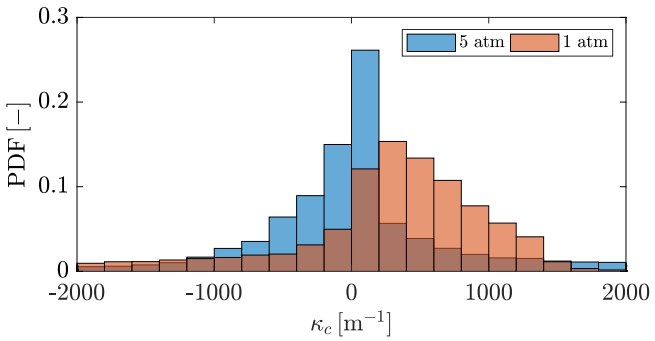

Fig. 5. Probability density function of the curvature value obtained along the whole flame front of the thermodiffusively unstable flames under atmospheric and elevated pressure conditions. The reference solutions correspond to the (different) time instants when both thermodiffusively unstable flames are fully developed, i.e., $t = 105.5\,\mathrm{ms}$ for the $p = 5\,\mathrm{atm}$ case and $t = 120\,\mathrm{ms}$ for the $p = 1\,\mathrm{atm}$ case.

To quantify the instantaneous distribution of the curvature, the probability density function (PDF) of the curvature value for the thermodiffusively unstable flame at the elevated pressure is calculated along the whole flame front, see Fig. 5. The PDF indicates the normalized probability of the curvature in a specific bin. Specifically, the PDF value in the ith bin corresponds to,

$$\mathrm{PDF}_i = \frac{c_i}{N} \times 100\% \tag{9}$$

where c_i is the number of elements in the ith bin, and N is the total number of elements extracted from the sample region. For comparison, the PDF of the thermodiffusively unstable flame under atmospheric conditions is superimposed. Note that the reference solutions shown in Fig. 5 correspond to the (different) time instants when both thermodiffusively unstable flames are fully developed, i.e., the flame radius at atmospheric pressure is about three times larger than that at elevated pressure, due to the larger critical flame radius and faster flame propagating speed. It is clearly seen that the magnitude of negative curvature at the elevated pressure is larger than that under atmospheric conditions. The strong negative curvature at elevated pressure poses a challenge to manifold methods such as flamelet. For the conventional tabulation model [56–58],

the flamelet table is generated based on the flamelet in physical space. However, the canonical flame configurations in physical space are known to be inherently unstable at a negative strain rate, e.g., the rearward stagnation flame [59]. Moreover, only a very limited range of curvature can be covered by a physical space flame due to geometrical restrictions, e.g., the minimum realizable nozzle radius. By comparison, the newly proposed composition space modeling method has the particular advantage that wider ranges of curvature and strain rate can be incorporated in the flamelet table, as already demonstrated in our previous works [53, 55]. The performance of the newly proposed composition space modeling method will be evaluated in Section 4.3.

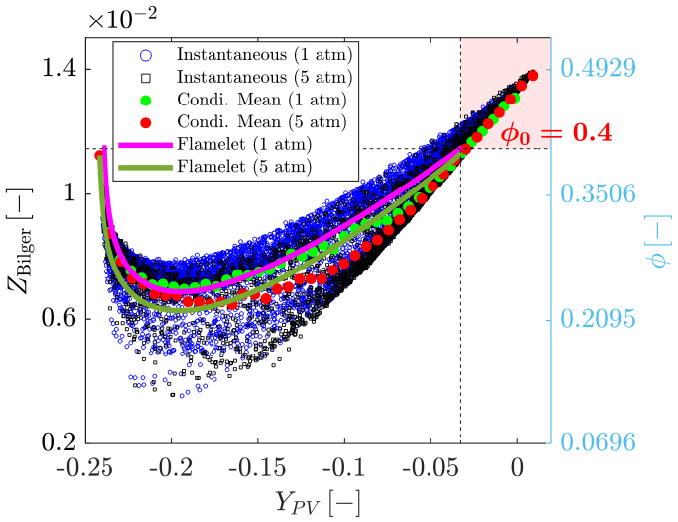

Fig. 6. Instantaneous distributions of the Bilger mixture fraction in the reaction progress variable space, comparing the atmospheric and elevated pressure conditions for the expanding unstable premixed flames studied. The filled circles indicate the corresponding conditioned values in the reaction progress variable space, while the corresponding flamelet solutions calculated under the same conditions as the reference simulation are superimposed for comparison, with strain rate and curvature set to zero. The vertical and horizontal dashed lines indicate the upper limits of the reaction progress variable and Bilger mixture fraction, respectively. The right y axis shows the equivalence ratio value corresponding to the Bilger mixture fraction shown on the left y axis, with the equivalence ratio of the unburnt H_2/air mixture ($\phi_0 = 0.4$) being indicated.

To quantify the effects of pressure on fuel stratification, the instantaneous distributions of the Bilger mixture fraction obtained from different pressure conditions are shown in the reaction progress variable space, see Fig. 6. The conditioned values are indicated as filled circles, while the flamelet solutions calculated under the same conditions as the reference simulation are superimposed for comparison, with the strain rate and curvature set to zero. Overall, the instantaneous distributions of the Bilger mixture fraction do not show strong differences between the atmospheric and elevated pressure conditions. Due to the strong strain rate and curvature in the thermodiffu-

sively unstable flames, the maximum value of the Bilger mixture fraction in the reference simulation is larger than that calculated from the flamelet solutions without the strain rate and curvature, as indicated by the colored region in the upper-right corner of Fig. 6. Moreover, the conditioned mean value of Z_{Bilger} at an elevated pressure is seen to be lower than that under the atmospheric conditions in the preheat zone, which is consistent with the corresponding flamelet solutions. This change in the Bilger mixture fraction distribution under different pressure conditions indicates that the dominating transport process could be different as the pressure changes. This will be clarified in the next subsection by a *budget* analysis.

Finally, the instability of the thermodiffusively unstable premixed hydrogen/air flame is examined using a linear stability analysis. The neutral stability curves obtained from Eq. (7) for the flames investigated at 5 atm and 1 atm are shown in Fig. 7a as the solid and dashed lines, respectively. The shaded zone indicates the unstable regime for the 5 atm case. The nose of the neutral stability curve, referred to as a peninsula [31], determines the critical Péclet number/flame radius and wavenumber/wavelength at the onset of instability. As indicated in the figure, the critical Péclet number Pe_c is 54, which corresponds to a critical flame radius of $R_c = Pe_c \cdot l_D = 21.6\,\text{mm}$, with the flame thickness l_D being 0.4 mm. This theoretical value is close to the reference solutions shown in Fig. 7c. At $t = 40.5\,\text{ms}$ (i.e., the black line with a flame radius of 20 mm), the entire flame surface is covered with corrugated cells. At a slightly earlier time instant, only tiny disturbances can be observed (i.e., the magenta line). According to the critical flame radius R_c and the critical wavenumber n_c, the critical wavelength/cell size can be determined as, $\Lambda_c = 2\pi R_c/n_c = 2.42\,\text{mm}$. Compared to the elevated pressure conditions, the critical Péclet number for the thermodiffusively unstable flame under atmospheric conditions is larger than that at the elevated pressure, suggesting that the fuel-lean hydrogen/air flame tends to be unstable at a smaller radius ($R_c = Pe_c \cdot l_D$) as the pressure increases. This is consistent with experimental results [11–13, 15, 19]. For the atmospheric conditions, the critical Péclet number predicted by the asymptotic theory is 68, which corresponds to a critical flame radius of 43.6 mm, with the flame thickness being 0.64 mm. This theoretical value is again close to the reference solutions. As shown in Fig. 7b, the cellular structure appears at $t = 27.5\,\text{ms}$ with $R \approx 41\,\text{mm}$. At the later time-instant with $R \approx 47\,\text{mm}$, cells with a significant amplitude of the disturbance can be observed.

From the neutral stability curve, the largest and smallest cell sizes can also be determined from the asymptotic lines of its lower and upper branches, respectively, as indicated by the blue and red lines in Fig. 7a. In fact, for different pressure conditions, the asymptotic wavenumber of the lower

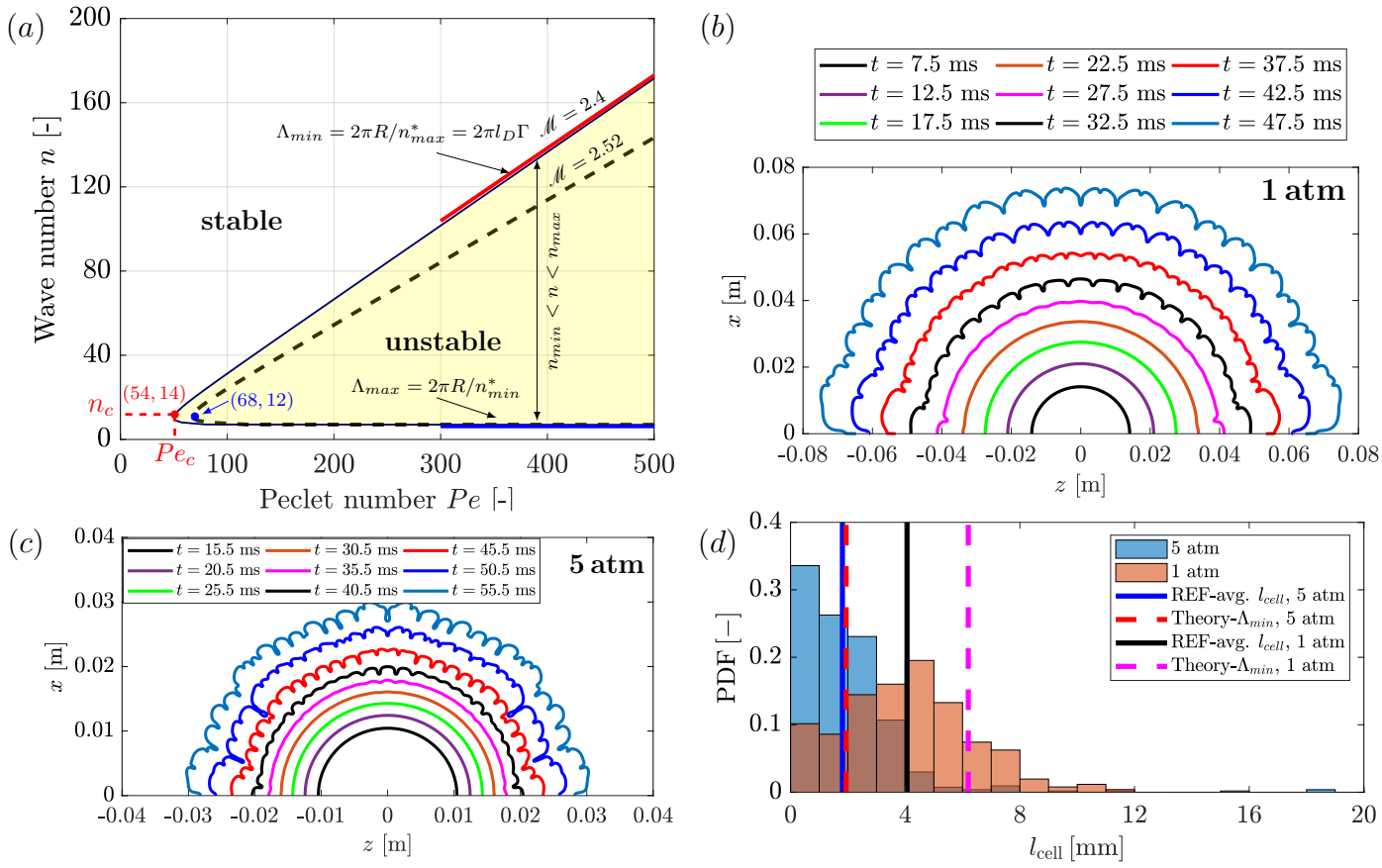

Fig. 7. (a) Neutral stability curves for the expanding premixed hydrogen flame at 5 atm (solid line) and 1 atm (dashed line) with an equivalence ratio of 0.4 and a temperature of 300 K, showing the wavenumber n as a function of Péclet number. The shaded zone indicates the unstable regime for the 5 atm case. The critical Péclet number, wavenumber and asymptotic lines for the 5 atm case are indicated. (b, c) Evolution of the flame front ($Y_{PV} = -0.11$) against time for the 1 atm and 5 atm cases, respectively, showing the critical flame radii. (d) Probability density function of the cell size obtained from the reference simulation for the 1 atm and 5 atm cases. The vertical solid line indicates the average cell size calculated from the reference simulation, while the vertical dashed line corresponds to the asymptotic theory. The reference solutions are extracted from single snapshots for both conditions at fully developed states, with the flame radius at the atmospheric pressure being three times larger than that at the elevated pressure.

branch n^*_{min} does not exhibit any obvious differences, i.e., $n^*_{min} \approx 6.2$ for the specific cases studied. Thus, the largest cell size Λ_{max} for different pressure conditions depends purely on the flame radius. On the other hand, the asymptotic wavenumber of the upper branch n^*_{max} is determined by the asymptotic line $Pe/n^*_{max} = \Gamma$, where Γ depends on the effective Lewis number, the Prandtl number, and the equivalence ratio, see Eq. (8). This corresponds to the limit of thermodiffusive instability of an unstable flame. Unlike the asymptotic values for the lower branches, the gradients of the asymptotic lines for the upper branches of the neutral stability curves are different as pressure

changes, which can be characterized by the unburnt Markstein number $\mathscr{M}$ [17, 18],

$$\mathscr{M} = \gamma_1 + \gamma_2 \mathscr{Z} \left(Le_{eff} - 1 \right) / 2 \tag{10}$$

where the formulations of γ_1 and γ_2 are given in the Supplementary Material. It is calculated that the Markstein number for the atmospheric conditions ($\mathscr{M} = 2.52$) is larger than that at the elevated pressure ($\mathscr{M} = 2.4$). We note that these $\mathscr{M}$ values are larger than those calculated by Matalon et al., see Fig. 2 in ref. [18], which could be due to the fact that different formulations are used to approximate the normalized thermal conductivity $\widetilde{\lambda}$ in calculation γ_1 and γ_2 in Eq. (10). For the specific conditions studied in this work, we find that the profile of $\widetilde{\lambda}$ can be fitted more accurately by a power-law expression with $\widetilde{\lambda} = \widetilde{T}^{0.62}$ than $\widetilde{\lambda} = \widetilde{T}^{0.5}$ in [18].

The distribution of the cell size l_{cell} in the reference simulation is quantified to compare with the asymptotic theory, as shown in Fig. 7d. The cell size l_{cell} is defined as the distance between two distinct neighboring peaks with negative curvature along the flame front, i.e., determined in the arc length l_{arc} space as shown in Fig. 4. The vertical sold line indicates the average cell size calculated from the reference simulation, while the vertical dashed line indicates the corresponding value calculated from the asymptotic theory. It is clearly seen that for the elevated pressure case, the average cell size calculated from the asymptotic theory agrees very well with that extracted from the reference solutions, while for the atmospheric case, the theoretical value is larger than that from the reference solutions. Overall, the average cell size at the elevated pressure is smaller than that under the atmospheric conditions due to enhanced intrinsic instabilities. We note that the different agreements of the averaged cell size between the reference simulation and the asymptotic theory for different pressure conditions could be related to the uncertainties in calculating the flame parameters involved in the asymptotic theory, such as the flame thickness, Lewis numbers, activation energy, etc. As reported by Beeckmann et al. [15], the flame thickness and the Lewis number can vary depending on the specific method used for calculation. For example, the flame thickness can be calculated according to the temperature gradient or the full width at half maximum reaction rate. Thus, we can only conclude that the flame parameters chosen here give good predictions for the elevated pressure condition, while discrepancy exists for the atmospheric condition.

4.2. Budget analysis of the generalized premixed flamelet equations in composition space

In this section, a *budget* analysis of the generalized premixed flamelet equations in composition space is conducted to identify the importance of different physical processes.

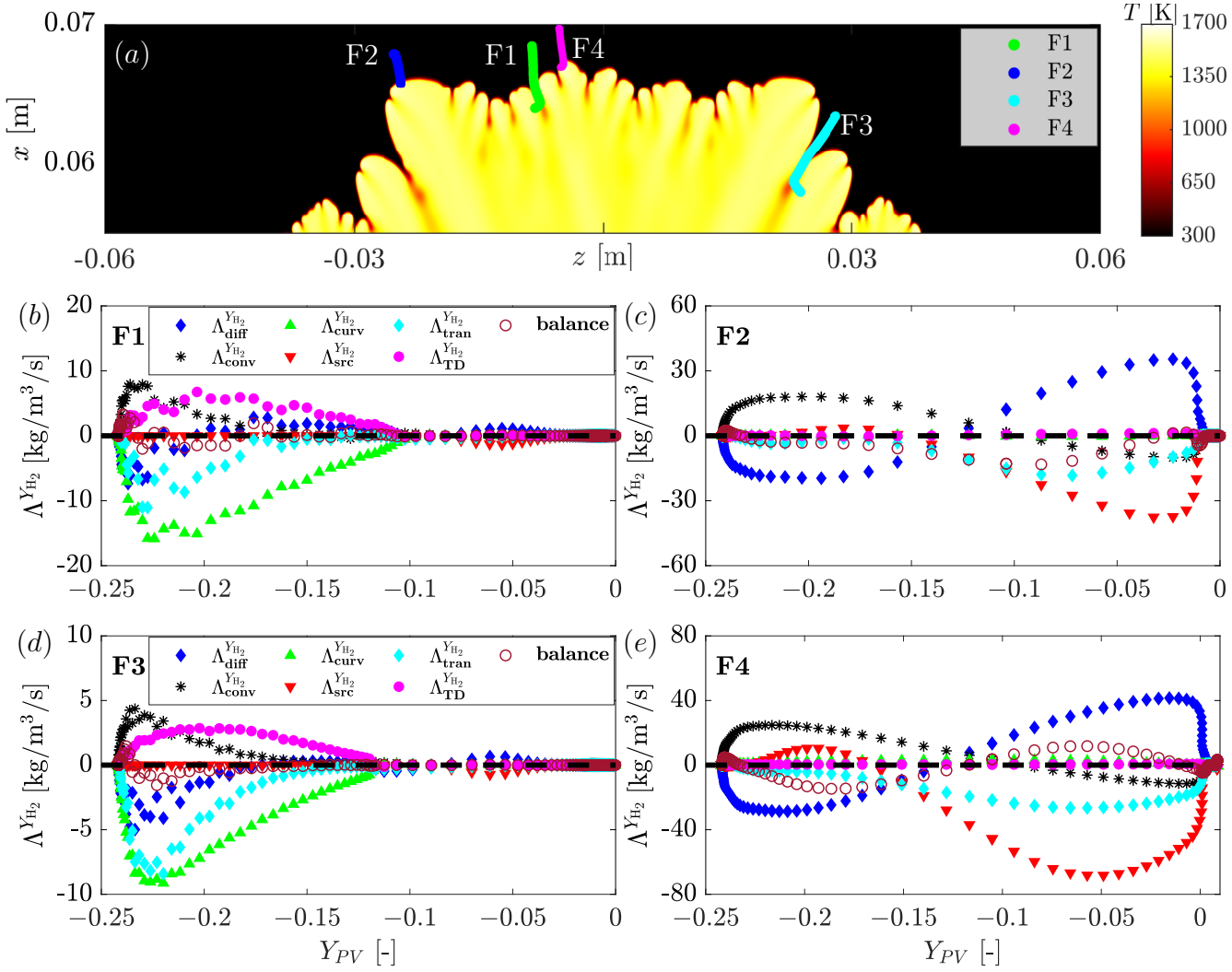

Fig. 8. (a) Four representative flamelets extracted from the reference simulation superimposed on the contour plot of temperature; (b-e) Comparing budget terms of H_2 mass fraction premixed flamelet equation in the reaction progress variable space, see Eq. (1), for the four representative flamelets. The balance term is calculated by subtracting the other terms from the transient term. The horizontal black dashed line indicates the location of zero value.

Figure 8 compares the budget terms of H_2 mass fraction premixed flamelet equations in the reaction progress variable space for four representative flamelets extracted from the reference simulation. The four flamelets, referred to as F1-F4, feature negative curvatures in the small cells (F1) and large cells (F3), negligible curvature (F2), and positive curvature (F4), as visualized in Fig. 8a of the contour plot of T. Here, the H_2 mass fraction is selected since it is the fuel species and has high diffusion velocity. The balance term is calculated by subtracting the other terms from the transient term. It is clearly seen that for the flamelets with negative curvature, i.e., F1 and F3, the curvature term $\Lambda^{Y_{H_2}}_{curv}$ is dominant compared to the other budget terms. In this case, the

tangential diffusion term $\Lambda_{\mathrm{TD}}^{Y_{\mathrm{H_2}}}$ is also important, and comparable or even larger than the normal diffusion term $\Lambda_{\mathrm{diff}}^{Y_{\mathrm{H_2}}}$, the convection term $\Lambda_{\mathrm{conv}}^{Y_{\mathrm{H_2}}}$ and the transient term $\Lambda_{\mathrm{tran}}^{Y_{\mathrm{H_2}}}$. This indicates that at cusps with negative curvature, the highly diffusive species tends to diffuse along the flame front from the neighboring high concentration regions, resulting in tangential diffusion. For the flamelet with negligible curvature, i.e., F2, both the curvature term $\Lambda_{\mathrm{curv}}^{Y_{\mathrm{H_2}}}$ and the tangential diffusion term $\Lambda_{\mathrm{TD}}^{Y_{\mathrm{H_2}}}$ are negligible, as expected. For the flamelet with positive curvature, i.e., F4, it is seen that the curvature term $\Lambda_{\mathrm{curv}}^{Y_{\mathrm{H_2}}}$ and the tangential diffusion term $\Lambda_{\mathrm{TD}}^{Y_{\mathrm{H_2}}}$ are also negligible compared to the other budget terms. Compared to the flamelets with negative curvature, where the reaction source term $\Lambda_{\mathrm{src}}^{Y_{\mathrm{H_2}}}$ is negligible, $\Lambda_{\mathrm{src}}^{Y_{\mathrm{H_2}}}$ is dominant in the flamelet with positive curvature, which mainly balances with the normal diffusion term $\Lambda_{\mathrm{diff}}^{Y_{\mathrm{H_2}}}$. From the above observations and the distributions shown in Fig. 4, it can be concluded that negative curvature tends to weaken the local reaction rate, while positive curvature tends to strengthen the local reaction intensity. The important characteristics of the representative flamelets with different curvatures are summarized in Table 1.

Table 1. Characteristics of the representative flamelets with different curvatures. The symbol $\bigoplus$ indicates the importance of the budget, while the symbol $\bigodot$ indicates that the budget is not important.

Flames	κ_c	$\Lambda_{\mathrm{curv}}^{Y_{\mathrm{H_2}}}$	$\Lambda_{\mathrm{TD}}^{Y_{\mathrm{H_2}}}$	$\Lambda_{\mathrm{src}}^{Y_{\mathrm{H_2}}}$
F1	$\ll 0$	$\bigoplus$	$\bigoplus$	$\bigodot$
F2	≈ 0	$\bigodot$	$\bigodot$	$\bigoplus$
F3	$\ll 0$	$\bigoplus$	$\bigoplus$	$\bigodot$
F4	$\gg 0$	$\bigodot$	$\bigodot$	$\bigoplus$

To clarify whether the dominant process for the intermediate species such as OH and O is the same as that for the H_2 species, the budget terms in the OH mass fraction premixed flamelet equation are compared in the reaction progress variable space in Fig. 9 for the representative flamelets. It is clearly seen that for the flamelets with negative curvature, i.e., F1 and F3, all the budget terms are close to zero, corresponding to $Y_{\mathrm{OH}} \approx 0$, see Fig. 3a. In contrast, for flamelets with negligible curvature (F2) and positive curvature (F4), the reaction source term $\Lambda_{\mathrm{src}}^{Y_{\mathrm{OH}}}$ and the transient term $\Lambda_{\mathrm{src}}^{Y_{\mathrm{OH}}}$ become dominant, and balance with each other. This indicates that the reaction rate dominates the local distribution of the intermediate species of OH in the thermodiffusively unstable flame. Comparing the magnitudes of the budget terms in F2 and F4 indicates that the positive curvature tends to strengthen the reaction rate of OH. The same

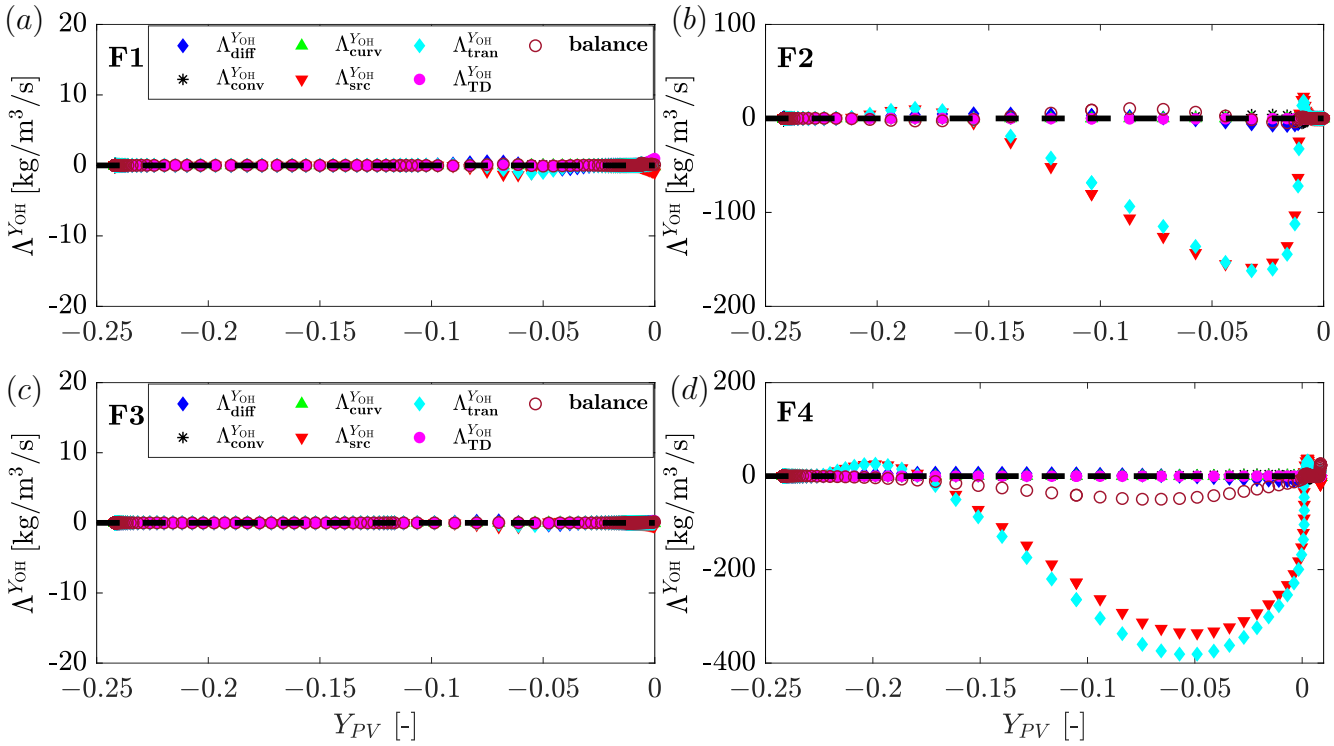

Fig. 9. Comparing budget terms of the Y_{OH} premixed flamelet equation in the reaction progress variable space, see Eq. (1), for the representative flamelets of (a) F1, (b) F2, (c) F3, and (d) F4. The balance term is calculated by subtracting the other terms from the transient term. The horizontal black dashed line indicates the location of zero value.

finding is obtained when comparing the budget terms for the O radical mass fraction, which is not shown here. The *budget* analyses for the intermediate species of OH and O indicate that the 1D assumption for the self-contained premixed flamelet equations is valid for these species since their tangential diffusion terms are negligible compared to the other budget terms. Comparing with the *budget* analysis shown in Fig. 8 indicates that the dominant process for the intermediate species of OH and O is different from that for the species of H_2.

Overall, the findings obtained from the *budget* analysis of the H_2 and OH radical mass fractions at the elevated pressure are consistent with the results for the atmospheric conditions. This also applies to the temperature and Bilger mixture fraction, which are not shown here. However, we note that this does not necessarily mean that the tangential diffusion processes at different pressure conditions are the same. Compared to the thermodiffusively unstable flame under the atmospheric conditions, the cellular structure spans a wider range of length scales, from small-scale cells to finger-like large-scale cells, which could result in different transport processes.

To illustrate the tangential diffusion process between cells with different length scales, Fig. 10

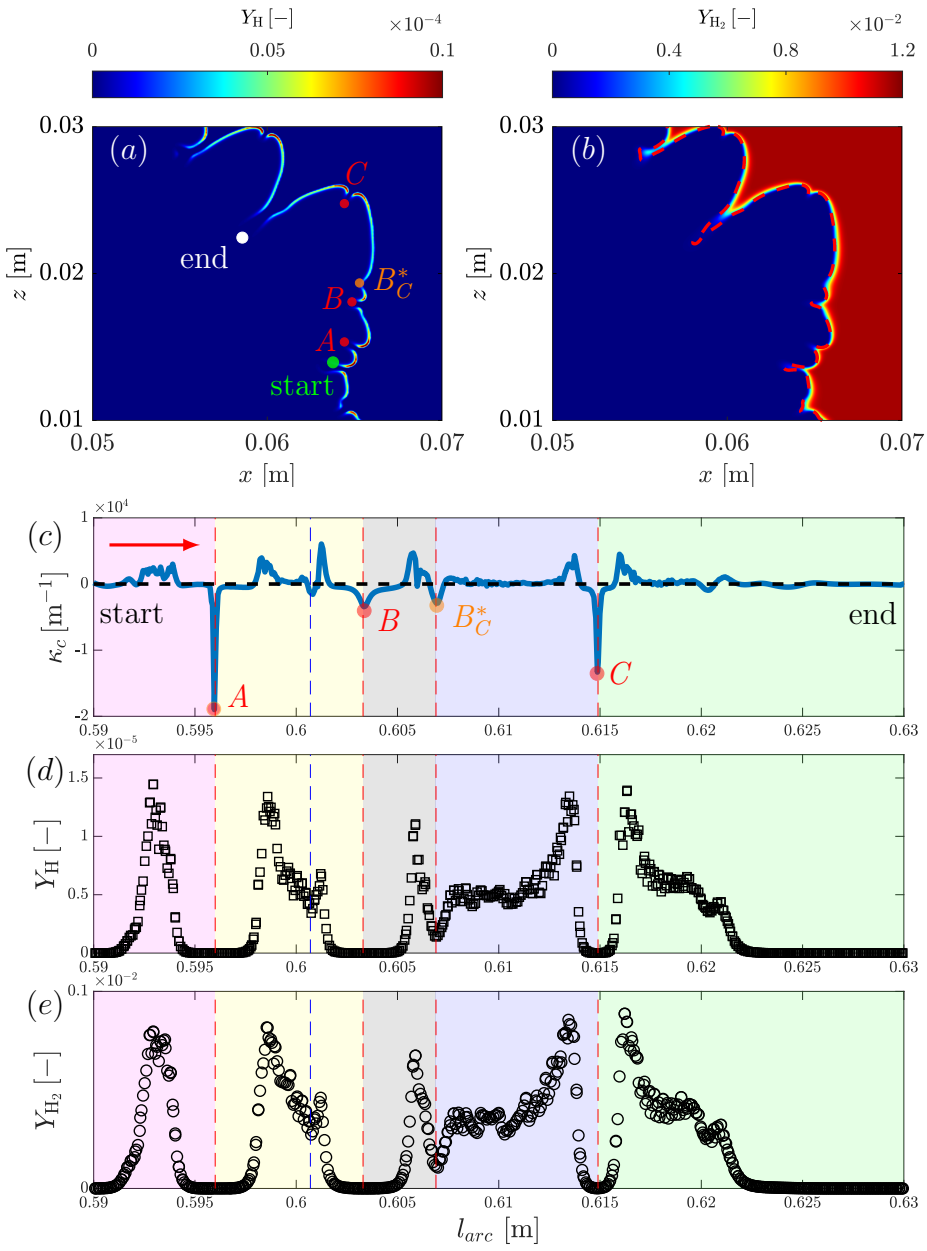

Fig. 10. (a,b) Contour plots of Y_{H} and $Y_{\mathrm{H_2}}$ in a selected region with cells of different length scales. The sample line from the starting point to the end point is indicated, along with the sample points with distinct negative curvature along the sample line. A representative iso-line of $Y_{PV} = -0.11$ in the reaction zone is indicated by a red dashed line in the contour plot of $Y_{\mathrm{H_2}}$. (c-e) Distributions of κ_c, Y_{H} and $Y_{\mathrm{H_2}}$ along the sample line. The background color shows the different cells. The indicated points A, B, B^*_C and C correspond to those shown in the contour plot of Y_{H}. The horizontal black dashed line in (c) indicates the location of $\kappa_c = 0$.

shows the distributions of the highly diffusive species of H and H_2 in a selected region with both finger-like large-scale cells and small-scale cells. The contour plots of Y_{H} and $Y_{\mathrm{H_2}}$ in the selected region are shown in Fig. 10a and 10b. The sample line from the starting point to the end point

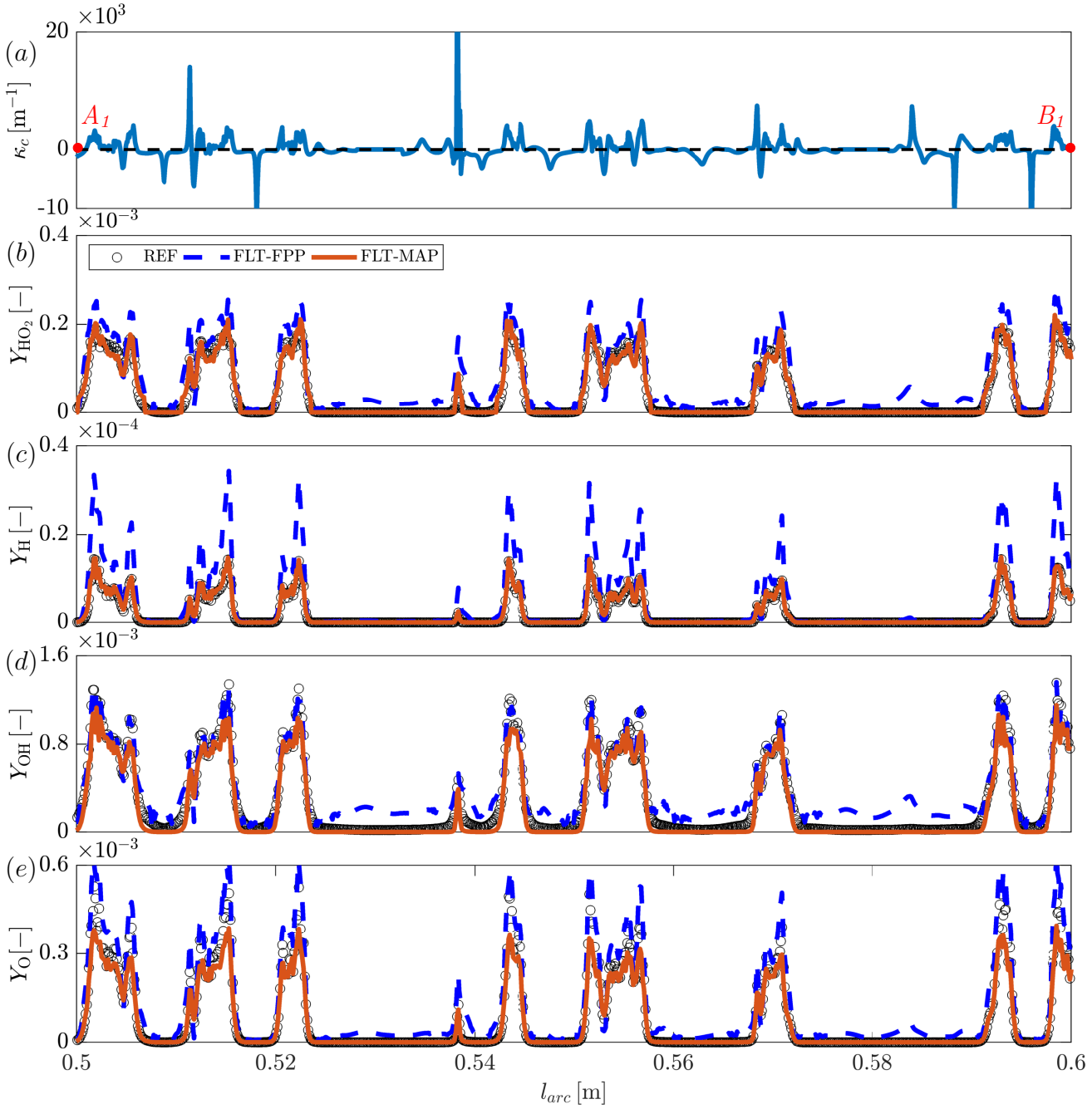

Fig. 11. Profiles of HO_2, H, OH, and O mass fractions along the isoline of $Y_{PV} = -0.11$ from point A_1 to point B_1, comparing the reference reference solutions with the FPP and MAP flamelet models. The selected corrugated flame front between point A_1 and point B_1 varies over a wide range of curvature values, see Fig. 3a. The corresponding curvature values of the flame front between A_1 and B_1 is shown in (a), with the horizontal dashed line being $\kappa_c = 0$.

is indicated, along with the sample points with distinct negative curvature along the sample line. Figure 10c-10e show the distributions of κ_c, Y_H and Y_{H_2} along the flame front within the sample line. The background color shows the different cells along the sample line. The sample points corresponding to those shown in the contour plot of Y_H are also indicated. It is seen that at point

A in a small cell with significant negative curvature, Y_{H} and $Y_{\mathrm{H_2}}$ are close to zero, which induces strong tangential diffusion from the neighboring peaks. The same phenomenon also applies to point B in a small cell, and point C in a large cell. The significance of tangential diffusion is determined by the gradient between the local valley and the neighboring peaks. It is noted that for a relatively small magnitude of negative curvature, as indicated by point B_C^*, the induced tangential diffusion could also be significant due to the neighboring peaks. Finally, we note that the cells are defined as the distance between two *distinct* neighboring peaks with negative curvature. A local peak with negligible negative curvature is not considered to be a cell, as indicated by the vertical blue line, although a local decrease in Y_{H} and $Y_{\mathrm{H_2}}$ can also be observed.

4.3. A priori analysis of the flamelet tabulation method

Compared with the thermodiffusively unstable flame under the atmospheric conditions shown in Part I [35], the flame investigated in this work at an elevated pressure is more challenging for flamelet modeling due to the wider ranges of strain rates and curvatures, and the thinner flame thickness. Thus, it is important to investigate whether the newly proposed flamelet tabulation method still works in this thermodiffusively unstable flame with enhanced hydrodynamic instability. The performance of the proposed tabulation method is evaluated based on an *a priori* analysis. Specifically, the trajectory variables in the flamelet look-up table (FLT) generated with premixed flamelet equations in composition space are calculated from the reference solutions, i.e., $\Psi^{\mathrm{MAP}}\left(Z_{\mathrm{Bilger}}^{\mathrm{REF}}, Y_{PV}^{\mathrm{REF}}, Y_{\mathrm{H}}^{\mathrm{str,REF}}, Y_{\mathrm{H}}^{\mathrm{cur,REF}}\right)$. The new composition space tabulation method is referred to as "FLT-MAP". For comparison, the conventional flamelet model based on the 1D freely propagating premixed (FPP) flame, with the FLT tabulated as, $\Psi^{\mathrm{FPP}}\left(Z_{\mathrm{Bilger}}^{\mathrm{REF}}, Y_{PV}^{\mathrm{REF}}\right)$, is also presented; this is referred to as "FLT-FPP". The essential difference between FLT-MAP and FLT-FPP is that wide ranges of strain rates and curvatures are inherently incorporated into the FLT-MAP, while neither effects can be taken into account in the FPP flamelet table.

The intermediate species, including HO_2, H, OH and O, which are difficult to predict using conventional combustion models, are compared, contrasting the tabulation methods of FLT-MAP and FLT-FPP and the reference simulation, see Fig. 11. Considering that the curvature value of the strongly corrugated flame front varies over a wide range of length scales, a representative segment of the curved flame front, from point A_1 to point B_1 in Fig. 3a, crossing significantly negative curvatures, is selected as a challenge for the flamelet model. It is clearly seen that the newly proposed flamelet tabulation method of FLT-MAP works better than the conventional

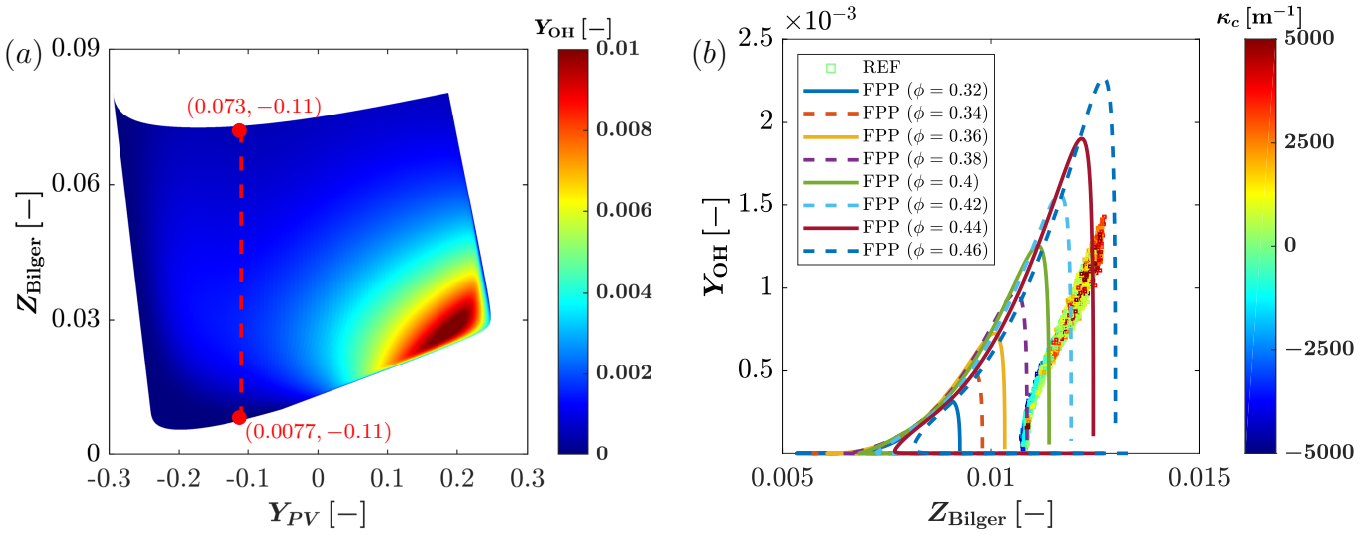

Fig. 12. (a) Flamelet data of the OH mass fraction in the (Z_{Bilger}, Y_{PV}) space, calculated based on the 1D freely propagating premixed (FPP) flames for different equivalence ratios obtained at $T_0 = 300\,\mathrm{K}$ and $p = 5\,\mathrm{atm}$ using the mixture-averaged approach. The vertical red dashed line corresponds to $Y_{PV} = -0.11$. (b) Instantaneous scatter data of the OH mass fraction extracted along the flame front (i.e., $Y_{PV} = -0.11$) from the reference solutions of the thermodiffusively unstable premixed hydrogen flame at elevated pressure condition. The solid and dashed lines correspond to the flamelet solutions at different equivalence ratios.

flamelet model of FLT-FPP in predicting the minor species mass fractions in regions with negative curvatures. Besides, the peaks of the HO_2 and H species, which correspond to the locations with positive curvatures, are also better predicted by the new FLT-MAP flamelet model. However, for the peaks of the OH and O species, the conventional FLT-FPP flamelet model gives better predictions than the FLT-MAP flamelet model. It is interesting to investigate why good predictions can be obtained by the FLT-FPP flamelet model with the strain rate and curvature effects being totally neglected in the flamelet table. For simplicity, we only take the OH mass fraction Y_{OH} as an example. Figure 12a shows the flamelet data of the OH mass fraction in the (Z_{Bilger}, Y_{PV}) space, calculated based on the 1D freely propagating premixed flames for various equivalence ratios at $T_0 = 300\,\mathrm{K}$ and $p = 5\,\mathrm{atm}$ using the mixture-averaged approach. As the profile of Y_{OH} in Fig. 11 is extracted along the flame front with a constant value of Y_{PV}, the range of Z_{Bilger} in the flamelet table can be determined, as indicated by the red dashed line. Figure 12b shows the instantaneous scatter data of the OH mass fraction extracted along the flame front (i.e., $Y_{PV} = -0.11$) from the reference simulation of the thermodiffusively unstable premixed hydrogen flame at elevated pressure condition. The local curvature value is color coded. It is seen that the OH mass fraction in the reference simulation can be covered by the flamelet look-up table within the corresponding

range of Z_{Bilger}. However, we note that the slightly better performance of the FLT-FPP flamelet model in predicting the peak values could be caused by the retrieval of peak values from the flamelet look-up table. More important, the local extinction states in regions with negative strain rate and curvature in general cannot be predicted by the FLT-FPP flamelet model because the strain rate and curvature information is neglected in the flamelet look-up table.

For the under-predictions of the peak values of the specific intermediate species with the new FLT-MAP flamelet tabulation method, there could be the following reasons. (1) The main reason for this could be due to the fact that the upper limit of the curvature in the reference simulation is not covered by the flamelet look-up table. Note that the peaks of the O and OH mass fractions correspond to the local peaks of the positive curvature, see Fig. 3a. In fact, for the thermodiffusively unstable premixed hydrogen flame at the elevated pressure condition, the upper limits of the strain rate and curvature are $1.3 \times 10^4\,\mathrm{s}^{-1}$ and $1.2 \times 10^5\,\mathrm{m}^{-1}$, respectively, at the investigated time-instant. In the flamelet table, the upper limits of the strain rate and curvature are $1.5 \times 10^4\,\mathrm{s}^{-1}$ and $6 \times 10^3\,\mathrm{m}^{-1}$, respectively. It can be observed that while the upper limit of strain rate can be covered by the flamelet look-up table, the upper limit of curvature is much smaller than that in the reference simulation. Due to the non-contained thermo-chemical states at large curvature, the peak values of the intermediate species mass fractions cannot be accessed from the flamelet look-up table. We note that the lower limits of the strain rate and curvature in the reference simulation can be covered by the flamelet look-up table since both conditions correspond to the flame quenching state, which has been considered when solving the self-contained flamelet equations, see the discussions in our previous work [55] on the extinction limit. The reason why the upper limit of the curvature in the reference simulation cannot be recovered by the self-contained strained-curved flamelet equations in composition space is considered as follows. In the self-contained flamelet equations, we assume that the flame structure is locally one-dimensional. However, for extremely high curvature, the flame thickness is close to the curvature length scale, i.e., the flame radius of $r_c = 1/\kappa_c$, which implies a flame kernel structure rather than a flame surface. In this case, the 1D assumption used to derive the self-contained flamelet equations is no longer valid, see also the discussions in our previous work [55] on the topological limit. The topological limit cannot be purely reflected in the tangential diffusion effects, but is more related to the transient effects. We note that except for the tangential diffusion terms, the *transient* terms are also not included in manifold creation and tabulation. In fact, at topological limit condition with extremely high curvature, the thermo-chemical states change rapidly over time, which can introduce transient

effects that cannot be reproduced by the adopted steady flamelets. Thus, the topological limit is expected to be characterized by the transient strained-curved flamelet equations. (2) The second reason that could lead to the discrepancy is due to the mapping technique. Note that the original flamelet solution in the (K_s, κ_c) space is an irregular domain, because for different values of K_s (or κ_c), the flamelet solutions may be converged at different ranges of κ_c (or K_s), see Fig. 2 in ref. [55]. However, a rectangular solution space is required to map the flamelet solutions between different spaces to avoid numerical issues [60, 61]. For the specific conditions studied in this work, a trimming of the flamelet solutions in the (K_s, κ_c) space is conducted, which limits the ranges of K_s and κ_c in the flamelet look-up table. The resulting range of curvature in the flamelet look-up table is less than that in the reference simulation for the elevated pressure condition. (3) The third reason could be related to neglecting tangential diffusion in the flamelet look-up table. Note that the self-contained generalized premixed flamelet equations are derived from the governing equations in physical space through coordinate transformation in a mathematically consistent way. Except for tangential diffusion, all the other physical processes have been considered in the self-contained premixed flamelet equations. The *budget* analysis for Y_{OH} premixed flamelet equation, see Fig. 9, shows that the tangential diffusion term is negligible for both negatively and positively curved flamelets. Thus, we think neglecting tangential diffusion cannot be the sole reason that leads to the inaccurate predictions of the peaks of Y_{OH}.

To address the three limitations of the proposed flamelet manifold method listed above, we propose the following guidelines for future research:

(i) Extending the flamelet table to include the unsteady states, which can potentially address the limitations of the proposed manifold method induced by the topological limit. However, we note that such an extension requires an additional trajectory variable for the flamelet manifold, which further increases the memory requirement of the associated table. In this regard, a novel technology, e.g., optimization strategy based on machine learning, would be feasible.

(ii) Utilizing normalized trajectory variables to parameterize the original flamelet solutions in the irregular domain, so that the trimming of the flamelet solutions to a rectangular space can be avoided. However, we note that the upper and lower limits in the normalization formulation for a specific trajectory variable depend on the values of the other trajectory variables. To overcome this issue, an iterative flamelet table look-up strategy, similar to the

"dual table look-up technique" for normalized total enthalpy [62] or for normalized reaction progress variable [63], is required, which however further increases the computational cost.

(iii) Incorporating the tangential diffusion effects in the flamelet table. This requires solving the strained-curved flamelet equations with additional tangential diffusion terms. It should be noted that the tangential diffusion terms are unclosed in the composition space, and new models should be proposed to incorporate the tangential diffusion effects in the 1D strained-curved flamelet equations.

5. Summary and conclusions

This work investigates an expanding premixed hydrogen flame at an elevated pressure by comprehensive analyses of the reference simulation, including a linear stability analysis from the asymptotic theory, a *budget* analysis and an *a priori* analysis. For the thermodiffusively unstable flame at an elevated pressure, the characteristics of the flame structure, the dominating physics of the cells with different curvatures, and the performance of the newly proposed tabulation method based on the flamelet equations in composition space are analyzed, quantified and evaluated, respectively. The main findings obtained in this work are summarized as follows:

(i) Compared to atmospheric conditions, the flame front is strongly corrugated over a wide range of length scales at an elevated pressure. The existence of strongly negative curvature in the small cell tends to lead to locally extremely fuel-lean conditions and local extinction;

(ii) The average cell size (wavelength) calculated with the asymptotic theory agrees very well with the value extracted from the reference simulation, particularly for the elevated pressure. For the lean premixed hydrogen/air flame investigated, the critical Péclet number at the elevated pressure is smaller than that at atmospheric pressure, indicating that the instability onset occurs at a smaller flame radius as the pressure increases;

(iii) For either small-scale cells or finger-like large-scale cells, the dominating transport contributions of the flamelets with negative and positive curvatures are similar for different pressure conditions. For the H_2 mass fraction in a negatively curved region, the curvature term and the tangential diffusion term are important, and balance with the transient term and the other transport processes. For the H_2 mass fraction in a positively curved region, the reaction source term is the most important, and balances with the normal diffusion term and the transient term, with the tangential diffusion term being negligible in comparison. For the

intermediate species of OH and O, all the budget terms are close to zero for negatively curved flamelets due to local extinction, while the reaction source term and the transient term are dominant in flamelets with negligible and positive curvatures.

(iv) The newly proposed tabulation method based on the premixed flamelet equations in composition space performs well in predicting the intermediate species in regions with negative curvature. While the peak values of some species mass fractions can be accurately predicted with the new flamelet model, they are under-predicted for specific species, such as OH and O. The reason for the under-prediction of the peak values of these species is mainly related to the fact that the upper limit of the curvature in the reference simulation is not covered by the flamelet look-up table due to the 1D assumption and the mapping technique.

Acknowledgments

The authors acknowledge the financial support provided by the German Research Foundation (DFG) - Project No. 411275182. This work was performed on the computational resource ForHLR II funded by the Ministry of Science, Research and the Arts Baden-Württemberg and the DFG. Arne Scholtissek acknowledges funding by the Fritz and Margot Faudi-Foundation - Project No. 55200502. Xu Wen acknowledges the financial support provided by the Alexander von Humboldt Foundation, and is grateful to Prof. Matalon and Prof. Law for sharing the materials and engaging in valuable discussions, and to Mr. Berger and Dr. Beeckmann for fruitful discussions on asymptotic theory.

References

[1] European Commission, available at https://eur-lex.europa.eu/legal-content/EN/TXT/?uri=CELEX:52020DC0301, 2020.

[2] S. Verhelst, T. Wallner, Hydrogen-fueled internal combustion engines, Prog. Energy Combust. Sci. 35 (2009) 490–527.

[3] S. E. Hosseini, B. Butler, An overview of development and challenges in hydrogen powered vehicles, Int. J. Green Energy 17 (2020) 13–37.

[4] H. L. Yip, A. Srna, A. C. Y. Yuen, S. Kook, R. A. Taylor, G. H. Yeoh, P. R. Medwell, Q. N. Chan, A review of hydrogen direct injection for internal combustion engines: towards carbon-free combustion, Appl. Sci. 9 (2019) 4842.

[5] The ETN Hydrogen Gas Turbines report — The path towards a zero-carbon gas turbine, available at https://etn.global/news-and-events/news/hydrogen-gas-turbines-report/, 2020.

[6] S. Verhelst, Recent progress in the use of hydrogen as a fuel for internal combustion engines, Int. J. Hydrog. Energy 39 (2014) 1071–1085.

[7] J. Yuan, Y. Ju, C. K. Law, On flame-front instability at elevated pressures, Proc. Combust. Inst. 31 (2007) 1267–1274.

[8] M. Klein, H. Nachtigal, M. Hansinger, M. Pfitzner, N. Chakraborty, Flame curvature distribution in high pressure turbulent bunsen premixed flames, Flow Turb. Combust. 101 (2018) 1173–1187.

[9] A. Attili, R. Lamioni, L. Berger, K. Kleinheinz, P. E. Lapenna, H. Pitsch, F. Creta, The effect of pressure on the hydrodynamic stability limit of premixed flames, Proc. Combust. Inst. 38 (2021) 1973–1981.

[10] H. Kobayashi, H. Kawazoe, Flame instability effects on the smallest wrinkling scale and burning velocity of high-pressure turbulent premixed flames, Proc. Combust. Inst. 28 (2000) 375–382.

[11] O. Kwon, G. Rozenchan, C. K. Law, Cellular instabilities and self-acceleration of outwardly propagating spherical flames, Proc. Combust. Inst. 29 (2002) 1775–1783.

[12] G. Rozenchan, D. L. Zhu, C. K. Law, S. D. Tse, Outward propagation, burning velocities, and chemical effects of methane flames up to 60 atm, Proc. Combust. Inst. 29 (2002) 1461–1470.

[13] C. K. Law, G. Jomaas, J. K. Bechtold, Cellular instabilities of expanding hydrogen/propane spherical flames at elevated pressures: theory and experiment, Proc. Combust. Inst. 30 (2005) 159–167.

[14] C. K. Law, Propagation, structure, and limit phenomena of laminar flames at elevated pressures, Combust. Sci. Technol. 178 (2006) 335–360.

[15] J. Beeckmann, R. Hesse, S. Kruse, A. Berens, N. Peters, H. Pitsch, M. Matalon, Propagation speed and stability of spherically expanding hydrogen/air flames: Experimental study and asymptotics, Proc. Combust. Inst. 36 (2017) 1531–1538.

[16] C. K. Law, S. Chaudhuri, F. Wu, Princeton Art of Science Gallery, available at https://www.princeton.edu/~artofsci/gallery2013/one.php%3Fid=383.html, 2013.

[17] R. Addabbo, J. Bechtold, M. Matalon, Wrinkling of spherically expanding flames, Proc. Combust. Inst. 29 (2002) 1527–1535.

[18] M. Matalon, C. Cui, J. Bechtold, Hydrodynamic theory of premixed flames: effects of stoichiometry, variable transport coefficients and arbitrary reaction orders, J. Fluid Mech. 487 (2003) 179.

[19] D. Bradley, M. Lawes, K. Liu, S. Verhelst, R. Woolley, Laminar burning velocities of lean hydrogen–air mixtures at pressures up to 1.0 MPa, Combust. Flame 149 (2007) 162–172.

[20] G. Darrieus, Propagation d'un front de flamme, La Technique Moderne 30 (1938) 18.

[21] L. Landau, On the theory of slow combustion, in: Dynamics of Curved Fronts, Elsevier, 1988, pp. 403–411.

[22] A. Istratov, E. Korovjanskaja, V. Librovich, On the stability of shock and detonation waves in arbitrary media, in: Symp. (Int.) Combust., volume 12, Elsevier, pp. 779–791.

[23] J. Bechtold, M. Matalon, Hydrodynamic and diffusion effects on the stability of spherically expanding flames, Combust. Flame 67 (1987) 77–90.

[24] S. Kadowaki, H. Suzuki, H. Kobayashi, The unstable behavior of cellular premixed flames induced by intrinsic instability, Proc. Combust. Inst. 30 (2005) 169–176.

[25] C. Altantzis, C. E. Frouzakis, A. G. Tomboulides, S. G. Kerkemeier, K. Boulouchos, Detailed numerical simulations of intrinsically unstable two-dimensional planar lean premixed hydrogen/air flames, Proc. Combust. Inst. 33 (2011) 1261–1268.

[26] C. Altantzis, C. Frouzakis, A. Tomboulides, M. Matalon, K. Boulouchos, Hydrodynamic and thermodiffusive instability effects on the evolution of laminar planar lean premixed hydrogen flames, J. Fluid Mech. 700 (2012) 329–361.

[27] C. E. Frouzakis, N. Fogla, A. G. Tomboulides, C. Altantzis, M. Matalon, Numerical study of unstable hydrogen/air flames: shape and propagation speed, Proc. Combust. Inst. 35 (2015) 1087–1095.

[28] L. Berger, K. Kleinheinz, A. Attili, H. Pitsch, Characteristic patterns of thermodiffusively unstable premixed lean hydrogen flames, Proc. Combust. Inst. 37 (2019) 1879–1886.

[29] G. K. Giannakopoulos, C. E. Frouzakis, S. Mohan, A. G. Tomboulides, M. Matalon, Consumption and displacement speeds of stretched premixed flames—Theory and simulations, Combust. Flame 208 (2019) 164–181.

[30] F. Creta, P. E. Lapenna, R. Lamioni, N. Fogla, M. Matalon, Propagation of premixed flames in the presence of Darrieus–Landau and thermal diffusive instabilities, Combust. Flame 216 (2020) 256–270.

[31] D. Bradley, C. Sheppart, R. Woolley, D. Greenhalgh, R. Lockett, The development and struc-

ture of flame instabilities and cellularity at low Markstein numbers in explosions, Combust. Flame 122 (2000) 195–209.

[32] M. Matalon, B. J. Matkowsky, Flames as gasdynamic discontinuities, J. Fluid Mech. 124 (1982) 239–259.

[33] N. Peters, Laminar diffusion flamelet models in non-premixed turbulent combustion, Prog. Energy Combust. Sci. 10 (1984) 319–339.

[34] J. van Oijen, A. Donini, R. Bastiaans, J. ten Thije Boonkkamp, L. de Goey, State-of-the-art in premixed combustion modeling using flamelet generated manifolds, Prog. Energy Combust. Sci. 57 (2016) 30–74.

[35] X. Wen, T. Zirwes, A. Scholtissek, H. Böttler, F. Zhang, H. Bockhorn, C. Hasse, Flame structure analysis and composition space modeling of thermodiffusively unstable premixed hydrogen flame — Part I: Atmospheric pressure, Combust. Flame (2021) submitted.

[36] C. Bekdemir, L. Somers, L. de Goey, Modeling diesel engine combustion using pressure dependent flamelet generated manifolds, Proc. Combust. Inst. 33 (2011) 2887–2894.

[37] J. van Oijen, L. de Goey, Modelling of premixed laminar flames using flamelet-generated manifolds, Combust. Sci. Technol. 161 (2000) 113–137.

[38] V. Mittal, H. Pitsch, A flamelet model for premixed combustion under variable pressure conditions, Proc. Combust. Inst. 34 (2013) 2995–3003.

[39] F. Ladeinde, Z. Lou, W. Li, The effects of pressure treatment on the flamelet modeling of supersonic combustion, Combust. Flame 204 (2019) 414–429.

[40] G. K. Giannakopoulos, A. Gatzoulis, C. E. Frouzakis, M. Matalon, A. G. Tomboulides, Consistent definitions of Flame Displacement Speed and Markstein Length for premixed flame propagation, Combust. Flame 162 (2015) 1249–1264.

[41] G. K. Giannakopoulos, M. Matalon, C. Frouzakis, A. G. Tomboulides, The curvature markstein length and the definition of flame displacement speed for stationary spherical flames, Proc. Combust. Inst. 35 (2015) 737–743.

[42] C. Altantzis, C. Frouzakis, A. Tomboulides, K. Boulouchos, Numerical simulation of propagating circular and cylindrical lean premixed hydrogen/air flames, Proc. Combust. Inst. 34 (2013) 1109–1115.

[43] P. E. Lapenna, L. Berger, A. Attili, R. Lamioni, N. Fogla, H. Pitsch, F. Creta, Data-driven subfilter modelling of thermo-diffusively unstable hydrogen–air premixed flames, Combust. Theor. Model. (2021) 1–22.

[44] A. Zschutschke, D. Messig, A. Scholtissek, C. Hasse, Universal Laminar Flame (ULF) solver, available at https://figshare.com/articles/ULF_code_pdf/5119855/2, 2017.

[45] T. Zirwes, F. Zhang, J. A. Denev, P. Habisreuther, H. Bockhorn, Automated code generation for maximizing performance of detailed chemistry calculations in OpenFOAM, in: High Performance Computing in Science and Engineering'17, Springer, 2018, pp. 189–204.

[46] F. Zhang, T. Baust, T. Zirwes, J. Denev, P. Habisreuther, N. Zarzalis, H. Bockhorn, Impact of infinite thin flame approach on the evaluation of flame speed using spherically expanding flames, Energy Technol. 5 (2017) 1055–1063.

[47] T. Zirwes, F. Zhang, P. Habisreuther, M. Hansinger, H. Bockhorn, M. Pfitzner, D. Trimis, Quasi-DNS dataset of a piloted flame with inhomogeneous inlet conditions, Flow Turbul. Combust. (2019) https://doi.org/10.1007/s10494--019--00081--5.

[48] T. Zirwes, T. Häber, F. Zhang, H. Kosaka, A. Dreizler, M. Steinhausen, C. Hasse, A. Stagni, D. Trimis, R. Suntz, et al., Numerical study of quenching distances for side-wall quenching using detailed diffusion and chemistry, Flow Turbul. Combust. 104 (2020) 997–1027.

[49] H. G. Weller, G. Tabor, H. Jasak, C. Fureby, A tensorial approach to computational continuum mechanics using object-oriented techniques, Comput. Phys. 12 (1998) 620–631.

[50] D. G. Goodwin, R. L. Speth, H. K. Moffat, B. W. Weber, Cantera: An object-oriented software toolkit for chemical kinetics, thermodynamics, and transport processes, available at https://www.cantera.org, 2018. Version 2.4.0.

[51] J. Hirschfelder, R. B. Bird, C. F. Curtiss, Molecular theory of gases and liquids (1964).

[52] T. Varga, T. Nagy, C. Olm, I. G. Zsély, R. Pálvölgyi, É. Valkó, G. Vincze, M. Cserháti, H. J. Curran, T. Turányi, Optimization of a hydrogen combustion mechanism using both direct and indirect measurements, Proc. Combust. Inst. 35 (2015) 589–596.

[53] A. Scholtissek, P. Domingo, L. Vervisch, C. Hasse, A self-contained composition space solution method for strained and curved premixed flamelets, Combust. Flame 207 (2019) 342–355.

[54] A. Scholtissek, P. Domingo, L. Vervisch, C. Hasse, A self-contained progress variable space solution method for thermochemical variables and flame speed in freely-propagating premixed flamelets, Proc. Combust. Inst. 37 (2019) 1529–1536.

[55] H. Böttler, A. Scholtissek, X. Chen, Z. Chen, C. Hasse, Premixed flames for arbitrary combinations of strain and curvature, Proc. Combust. Inst. 38 (2021) 2031–2039.

[56] Y. Xuan, G. Blanquart, M. E. Mueller, Modeling curvature effects in diffusion flames using a laminar flamelet model, Combust. Flame 161 (2014) 1294–1309.

[57] J. Schlup, G. Blanquart, Reproducing curvature effects due to differential diffusion in tabulated chemistry for premixed flames, Proc. Combust. Inst. 37 (2019) 2511–2518.

[58] M. U. Göktolga, P. de Goey, J. van Oijen, Modeling curvature effects in turbulent autoigniting non-premixed flames using tabulated chemistry, Proc. Combust. Inst. 38 (2021) 2741–2748.

[59] C. Law, C. Sung, Structure, aerodynamics, and geometry of premixed flamelets, Prog. Energy Combust. Sci. 26 (2000) 459–505.

[60] C. Hasse, N. Peters, A two mixture fraction flamelet model applied to split injections in a di diesel engine, Proc. Combust. Inst. 30 (2005) 2755–2762.

[61] X. Wen, H. Wang, Y. Luo, K. Luo, J. Fan, Evaluation of flamelet/progress variable model for laminar pulverized coal combustion, Phys. Fluids 29 (2017) 083607.

[62] X. Wen, M. Rieth, A. Scholtissek, O. T. Stein, H. Wang, K. Luo, A. M. Kempf, A. Kronenburg, J. Fan, C. Hasse, A comprehensive study of flamelet tabulation methods for pulverized coal combustion in a turbulent mixing layer Part I: A priori and budget analyses, Combust. Flame 216 (2020) 439–452.

[63] D. Messig, M. Vascellari, C. Hasse, Flame structure analysis and flamelet progress variable modelling of strained coal flames, Combust. Theor. Model. 21 (2017) 700–721.